An Exploration of Substrates for Surface-Enhanced Raman Scattering

by

Jason Robert Anema
B.Sc., University of Manitoba, 1999

A Dissertation Submitted in Partial Fulfillment
of the Requirements for the Degree of

DOCTOR OF PHILOSOPHY

in the Department of Chemistry

Supervisory Committee

An Exploration of Substrates for Surface-Enhanced Raman Scattering

by

Jason Robert Anema
B.Sc., University of Manitoba, 1999

Supervisory Committee

Dr. Alexandre Brolo (Department of Chemistry)
Supervisor

Dr. Natia Frank (Department of Chemistry)
Departmental Member

Dr. Matthew Moffitt (Department of Chemistry)
Departmental Member

Dr. David Sinton (Department of Mechanical Engineering)
Outside Member

Abstract

Supervisory Committee

Dr. Alexandre Brolo (Department of Chemistry)
Supervisor

Dr. Natia Frank (Department of Chemistry)
Departmental Member

Dr. Matthew Moffitt (Department of Chemistry)
Departmental Member

Dr. David Sinton (Department of Mechanical Engineering)
Outside Member

Surface-enhanced Raman scattering (SERS) constitutes a spectroscopy of rapidly growing importance. To understand and control the enhancing surface is key for optimizing SERS. In this work, progressively more ordered substrates for SERS are investigated: gold clusters, scratched gold films, nanohole arrays in a copper film and nanoscale gratings in a gold film.

Gold clusters constitute the most random SERS substrate: samples were prepared by alternating vapour deposition of gold and plasma-induced polymerization of styrene gas. The relationships between sample preparation parameters, gold-cluster morphology, and SERS intensity were elucidated. Using Wilson's notation, vibrations were assigned to all bands between 250 and 1750 cm^{-1} in the ordinary Raman and SERS spectra of polystyrene. The orientation of polystyrene's phenyl ring, relative to the gold surface, was determined. It has been suggested that reactions involving silver catalyze polystyrene degradation during SERS, but we found that silver is not necessary for the degradation to occur.

Of intermediate order are scratched gold films. Polarization-dependent SERS was studied for scratched gold films placed *in-situ* and under electrochemical control. A quantitative method for evaluating the polarization dependence was developed. In addition, we established that polarization effects may be used to selectively remove solution-phase interference signals from the SERS spectrum of an adsorbed analyte.

Nanohole arrays and nanoscale gratings, made by focused ion beam (FIB) milling, constitute the most ordered SERS substrates.

SERS was observed for oxazine 720 molecules adsorbed on a copper film pierced by nanohole arrays. Each of the arrays had a different hole-periodicity, and the effect of this periodicity on SERS intensity was examined. Electric fieldstrength perpendicular to the surface of the metal was calculated for each array using the finite-difference time-domain (FDTD) method, and the array with the greatest calculated value matched the array that gave the greatest experimentally observed SERS intensity.

Finally, SERS was observed for oxazine 720 molecules adsorbed on a gold film through which nanoscale gratings were milled. We varied the width of the grooves and the width of the metal lines between them, and we examined the resulting effect on SERS intensity.

Table of Contents

List of Tables

List of Figures

Acknowledgements

I wish to thank:

- My supervisor, Alexandre Brolo, for help with experimental and theoretical aspects of the work presented in this dissertation.
- All of my coworkers in the Brolo research group, for general assistance and for providing an enjoyable work atmosphere. Meikun Fan, Marcos Santos and Gabriele Hager for helpful discussions which had a significant impact on this research.
- Alexandre Felten and Carla Bittencourt, who collaborated with me on the polystyrene/gold-cluster samples project.
- UVic's machine shop, for making the electrochemical cell used in the scratches project.
- Kiran Swaroop Kumar and Li Yang, for assistance with practical issues involving the FIB.
- Pramodha Marthandam and Reuven Gordon, who collaborated with me on the nanohole arrays project. Laura Han Li and Jack Anema, for assistance with computer code used to mill the nanohole arrays.
- Mohammad Rahman, Samantha Grist and Karen Kavanagh who collaborated with me on the nanoscale gratings project.
- NSERC, UVic, CFI and BCKDF for funding.

Chapter 1: INTRODUCTION

1.1 The Raman Effect

1.1.1 Discovery

The inelastic scattering of light was proposed on theoretical grounds by Smekal in 1923.[1] Experimental observation of this was first reported by Raman, together with Krishnan, in 1928.[2] Raman's work was verified by others in the same year;[3,4] and by the end of 1928, about sixty papers were published on the subject.[5] In 1930, Raman was awarded the Nobel Prize in physics for discovering the effect which bears his name.

1.1.2 A Basic Description of the Raman Effect

In Raman spectroscopy, energy transfer occurs while a photon of visible light is scattered by a molecule.[5,6] The scattered photon may have less (Stokes shifted) or more (anti-Stokes shifted) energy than the incident photon, and this difference corresponds to a change in the vibrational state of the molecule. Energy transfer from the photon to the molecule is more probable statistically, and the spectroscopy of Stokes shifted light is usually employed. Raman scattering is diagrammed schematically in Figure 1.1. The energy of the incident photon is given by $h\nu_0$, the energy of the molecular vibration is given by $h\nu_{vib}$, v_0 represents the ground state vibrational level and v_1 represents the first excited vibrational level.

A normal mode of vibration is the movement of a particular group of atoms within a molecule. All atoms in the group move with the same vibrational frequency. Each normal mode may be excited independently of the others, and the actual vibrational motion of a molecule may be described as a linear combination of its normal modes. A nonlinear molecule consisting of N atoms has 3N-6 normal modes.[6] This is because each atom lies in 3-dimensional space and therefore has 3 degrees of freedom, except that the collective motion of all the atoms yields translation of the entire molecule in 3 cases and rotation of the entire molecule in 3 cases. A linear molecule has 3N-5 normal modes[6] because rotation of the entire molecule occurs in only 2 cases (rotation about the internuclear axis is meaningless for a linear molecule).

In order for a normal mode to be Raman active, the polarizability of the molecule must change during the vibration.[5,6] This means that either the size or the shape, or in some cases the orientation, of the molecule's electron cloud must change during the vibration.[6] Mathematically,

$$\left(\frac{\partial \alpha_m}{\partial Q}\right)_0 \neq 0 \tag{1.1}$$

where α_m is the polarizability of the molecule, Q is a normal coordinate, and $\partial\alpha_m/\partial Q$ is evaluated at the equilibrium position which is denoted by the subscript 0.[6]

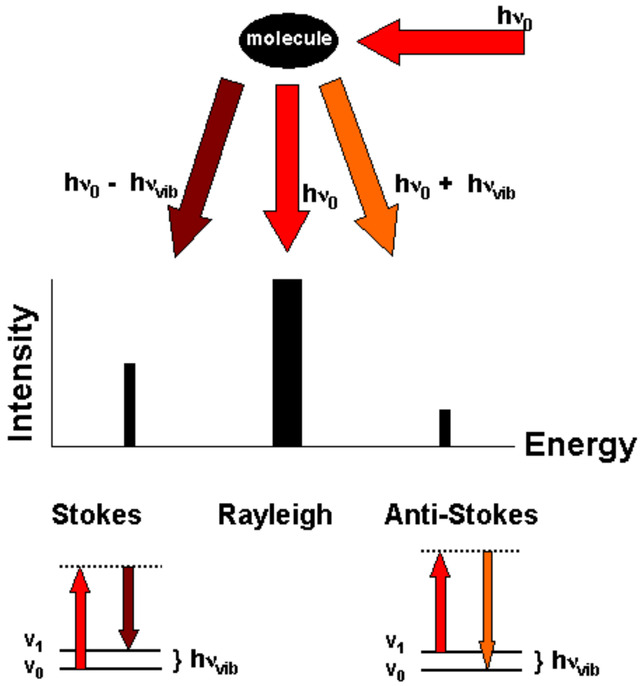

Figure 1.1 Raman scattering of light by a molecule.

1.1.3 Resonance Raman

Ordinary Raman scattering occurs by way of an unallowed energy level which is called a “virtual state”[7] (the dashed lines in Figure 1.1 represent virtual states). In resonance Raman scattering, the molecule is instead excited to an upper electronic state.[5,6] When the energy of the incident photon matches that required for an electronic transition, the probability of Raman scattering is increased by 3 to 5 orders of magnitude.[6]

1.2 Surface-Enhanced Raman Scattering (SERS)

1.2.1 Discovery

In 1974, Fleischman et al observed high-intensity Raman scattering by pyridine adsorbed on electrochemically roughened silver.[8] However, they did not acknowledge it as a new phenomenon. They had increased the surface area of the silver by roughening it, and they believed that the enhancement was simply due to an increase in the amount of pyridine on this larger surface.

Van Duyne et al[9] and Creighton et al[10] recognized that the increase in surface area was insufficient to account for the increased Raman intensity, and in 1977, they independently proposed that the surface played an essential role in the mechanism of enhancement.

1.2.2 A Basic Description of the SERS Effect

The intensity of Raman scattering is commonly enhanced by 5 or 6 orders of magnitude[11] when a Raman-active compound is adsorbed on the nanostructured surface of a free-electron metal (silver, gold and copper are primarily used[12,13]). Two mechanisms contribute to the SERS effect, one electromagnetic (EM)[11-14] and one chemical (charge transfer or CT)[11-15] in nature. It is generally agreed, however, that the EM mechanism is dominant under conditions used to carry out most SERS experiments.

1.2.3 The Electromagnetic (EM) Mechanism

Surface plasmons (SPs) are fluctuations in electron density which occur at the surface of a free-electron metal.[16,17] They are excited by visible light, oscillate in resonance with it, and result in localized regions at the surface where electromagnetic fieldstrength is greatly enhanced. The associated field is limited to a few hundred nm from the surface of the metal (typically around half the wavelength of the exciting radiation), and it decays exponentially over this distance.[16] SP propagation length (parallel to the surface) may range from microns to hundreds of microns depending on the type of metal and the excitation wavelength.[16]

Let us begin by examining the simplest SERS substrate: a single sphere of silver, gold or copper. Under appropriate conditions, light incident upon the sphere will displace electrons and initiate an oscillating dipole (i.e., form SPs). If a Raman-active molecule is close to the surface of the sphere, the SPs will initiate a dipole in the molecule.[12] Energy may then be lost to (or gained from) vibrational modes of the molecule, thus up-shifting (or down-shifting) the oscillation frequency of the molecule. At this point, emission of light may occur from the molecule and this emission would provide one contribution to the SERS signal.[12] In this case, SERS intensity is proportional to g^2:

$$I_{SERS} \propto g^2 \tag{1.2}$$

where g is the field enhancement averaged over the surface of the particle.[13] The mathematical definition of g is given by

$$g = \frac{\varepsilon_1 - \varepsilon_2}{\varepsilon_1 + 2\varepsilon_2} \tag{1.3}$$

where ε_1 is the permittivity of the metal comprising the sphere and ε_2 is the permittivity of the dielectric material surrounding the sphere.[11,12,18] Alternatively, the molecular dipole can influence the sphere's dipole before emission takes place.[12] Then emission of light may occur from the sphere after it begins to oscillate with the shifted frequency of the molecule, and this emission would provide another contribution to the SERS signal.[12] In this latter case, the particle enhances the outgoing as well as the incoming light intensity, and[13]

$$I_{SERS} \propto g^4 \qquad (1.4)$$

The effect of the molecular dipole on the sphere's dipole is most efficient when the frequency shift is small. Hence the fourth power relationship given by Equation 1.4 holds true only for small frequency shifts, and I_{SERS} is diminished for large shifts.[13]

A sphere's polarizability, α_s, scales with its radius, r, according to[13,19]

$$\alpha_s = r^3 \frac{\varepsilon_1 - \varepsilon_2}{\varepsilon_1 + 2\varepsilon_2} \qquad (1.5)$$

For a given metal in a given dielectric, some range of r values will be suitable for excitation of a dipole. Larger spheres will be too "soft" and form higher multipoles which do not efficiently enhance Raman activity.[13] Smaller spheres will be too "hard", and the movement of electrons at the surface of the sphere will be damped.[13] Equation 1.5 also reveals that, for an isolated sphere, a resonance exists when the real part of a metal's permittivity is $-2\varepsilon_2$. The imaginary part of a metal's permittivity determines SP efficiency: when it's large, more energy is lost as heat in the metal. The ideal size of a single, coinage metal sphere is 10 to 100 nm.[13]

Increasing the complexity of the SERS substrate, we now consider a single ellipsoidal particle: prolate (cigar-shaped, with one major axis and two minor axes) or oblate (coughdrop-shaped, with two major axes and one minor axis). Polarizability along a major axis will be greater than polarizability along a minor axis; therefore the orientation of the ellipsoid relative to the incident radiation will determine the efficiency with which a dipole SP may be excited.[6,12]

In addition to this orientation-dependent polarizability effect, ellipsoids display what has been termed the "lightning rod" or the "antenna" effect. In areas of high curvature, electromagnetic fieldstrength is consistently higher than the surface average.[12]

Enhancement due to this effect is significant: 2×10^4 times (and this number is multiplicative with dipole SP based enhancement) for molecules adsorbed at the tip of a 3:1:1 aspect-ratio prolate.[12,20]

Further increasing the complexity of the SERS substrate, we examine a pair of interacting spheres. If light is polarized along the intersphere axis, and if the spheres are sufficiently close together, then each sphere's light-induced dipole will enhance the other's by through-space electromagnetic coupling (Figure 1.2a).[13] Raman signal enhancement may reach ~ 11 orders of magnitude for a molecule located between two spheres, 0.5 nm from each.[13,21] This is ~ 6 orders of magnitude greater than the enhancement obtained from a molecule the same distance from an isolated sphere.[13,21] If light is polarized across the intersphere axis, Raman signal enhancement will be about the same as it would be if there was only one sphere; and this is true even if the molecule is located proximal to a region where fieldstrength is maximized (Figure 1.2b).[13,22]

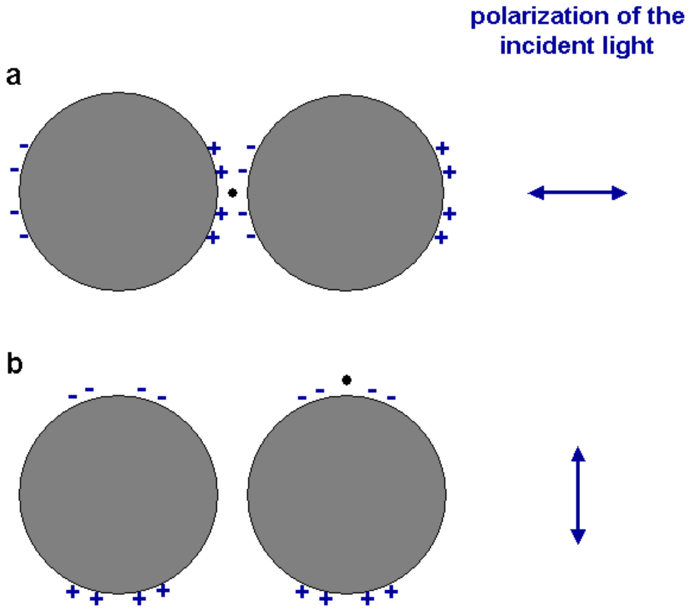

Figure 1.2 A SERS substrate composed of two spheres.

1.2.4 The SERS Selection Rule

Based on the EM mechanism of enhancement, a selection rule has been derived for SERS.

For molecules adsorbed on the surface of a single sphere sized appropriately for a dipole response to incident radiation, the effective Raman polarizability tensor (that which accounts for enhancement) is given by[23]

$$\boldsymbol{\alpha}_{eff} = \frac{9}{(\varepsilon_{1i}+2)(\varepsilon_{1R}+2)}\begin{bmatrix} \alpha_{\mathrm{xx}} & \alpha_{\mathrm{xy}} & \varepsilon_{1R}\alpha_{\mathrm{xz}} \\ \alpha_{\mathrm{yx}} & \alpha_{\mathrm{yy}} & \varepsilon_{1R}\alpha_{\mathrm{yz}} \\ \varepsilon_{1i}\alpha_{\mathrm{zx}} & \varepsilon_{1i}\alpha_{\mathrm{zy}} & \varepsilon_{1i}\varepsilon_{1R}\alpha_{\mathrm{zz}} \end{bmatrix} \qquad (1.6)$$

Here, as in Equation 1.3 and Equation 1.5, ε_1 is the permittivity of the metal comprising the sphere. The permittivity of a metal is dependent upon the frequency of the radiation interacting with it, therefore *i* and *R* are used to denote incident and Raman scattered frequencies. The x- and y-coordinates lay tangent to the surface of the sphere, and the z-coordinate lies normal to it.

If the frequency shift is small, $\varepsilon_{1R} \sim \varepsilon_{1i} = \varepsilon$. Since Raman intensity scales with the square of a polarizability tensor,[18,24] enhancement ratios of $1 : \varepsilon^2 : \varepsilon^4$ are predicted for vibrational modes which transform as α_{xx}, α_{yy}, α_{xy} : α_{xz}, α_{yz} : α_{zz}. In other words, preferential enhancement is predicted for vibrational modes with a polarizability change normal to the surface.

It is worth noting that this selection rule, derived by Creighton[23] using Equation 1.6, has also been derived by Moskovits[11,18] using the relationship between fieldstrength, E, and field enhancement averaged over the surface of a particle, *g*.

1.2.5 The Charge Transfer (CT) Mechanism

Certain aspects of SERS cannot be explained by the EM mechanism alone, and the CT mechanism[11-15] may be used to account for them. For example, CO and N_2 have similar polarizabilities but SERS intensity is 200 times greater for CO than it is for N_2 under the same experimental conditions.[14]

The CT mechanism involves formation of a metal-molecule complex, and enhancement occurs through a resonance Raman type of effect (Figure 1.3). Let us say that the highest occupied molecular orbital (HOMO) to lowest unoccupied molecular orbital (LUMO) electronic energy gap for an organic adsorbate corresponds to absorption of UV light with $\lambda \sim 300$ nm. If the Fermi level of the metal lies half way between, then the HOMO to Fermi level and Fermi level to LUMO energy gaps correspond to absorption of visible light with $\lambda \sim 600$ nm. Thus an electronic transition may lie in resonance with the excitation energy provided by a He-Ne laser ($\lambda = 633$ nm), which is often used for SERS.

The reason why CO and N_2 are enhanced to different extents, though they have similar polarizabilities, may now be understood: a metal-molecule complex which allows for the CT mechanism is formed in the case of CO but not in the case of N_2.

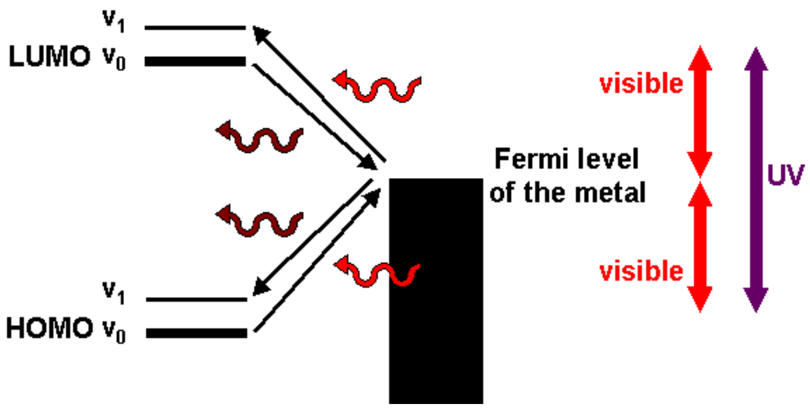

Figure 1.3 The charge transfer (CT) mechanism for SERS.

1.3 SERS Substrates

1.3.1 Classic SERS Substrates

The classic SERS substrates possess little order. They include electrochemically roughened surfaces, island films, and nanoparticle aggregates.

SERS was first observed, in 1974 by Fleischman et al, from pyridine adsorbed on electrochemically roughened silver[8] (the discovery of SERS is recounted in section 1.2.1). Electrochemical roughening involves oxidation-reduction cycling (ORC). Metal atoms are converted to ions during the oxidation half-cycle, and they enter the aqueous electrolyte solution. Metal atoms are reformed from the ions during the reduction half-cycle, and they are deposited onto the electrode surface. Suggested procedures, for silver and gold electrodes, have been offered in a recent review by Ren and Tian et al.[25] SERS substrates generated by ORC yield enhancement factors of about 10^6.[26]

Island films are prepared by the high-temperature evaporation of a metal onto a substrate (often glass). A set of oblate to prolate hemispheroids (they are truncated where they contact the substrate), separated by regions of bare substrate, are produced as a result of the competition between adatom mobility and crystallization. Island films yield enhancement factors of about 10^2 - 10^5.[27-29]

Nanoparticles are made by the chemical reduction of a metal salt which is dilute in aqueous solution. Aggregation may be induced by a number of methods; e.g., by adding a salt or by removing the aqueous solution. Of the three classic SERS substrates, this one (nanoparticle aggregates) is most actively being explored today. For example, nanoparticles have been tethered to one another and tethered to surfaces.[26] The goal of current activity is to improve SERS measurement reproducibility and/or SERS enhancement. Experiments employing nanoparticle aggregates have yielded enhancements as high as 10^{14} or 10^{15} [30,31] (there can be no doubt that these large enhancements were obtained from aggregated rather than isolated nanoparticles;[13] we note also that there was a resonance Raman contribution in the case of reference 31 but not in the case of reference 30 [14,32]).

1.3.2 Modern SERS Substrates

Modern SERS substrates generally possess more order than the classic ones. They are engineered to improve SERS measurement reproducibility and/or SERS enhancement. Some of the modern techniques used to create SERS substrates include nanoparticle tethering, nanosphere lithography (NSL), electron beam lithography (EBL), and focused ion beam (FIB) milling.

Vlčková and Moskovits et al used 4,4'-diaminoazobenzene as a tether while creating silver nanoparticle dimers, and 3-aminopropyltrimethoxysilane to link the dimers to a transmission electron microscopy (TEM) finder grid.[33] SERS was observed from single 4,4'-diaminoazobenzene molecules, which would automatically place themselves in the

SP hotspot while acting as a tether. The specific nanoparticle dimer yielding single-molecule SERS could be located and imaged using the finder grid and TEM.

In NSL,[34,35] a smooth surface is covered with a solution of polymer nanospheres and the spheres self-assemble in a 2-D hexagonal closest packed arrangement. Metal is deposited onto the spheres, and the resulting "film over nanospheres (FON)" can be SERS-active (FONs have been used to make SERS-based sensors for glucose[36] and an anthrax biomarker[37]). Alternatively, the metal-coated spheres may be removed, exposing an array of truncated tetrahedra formed by deposition of metal in the voids between the spheres. Arrays of truncated tetrahedra can also be SERS-active.

In EBL,[34,35] some photoresist material is modified by exposure to a beam of electrons. During subsequent developing, either exposed or unexposed portions of the photoresist are selectively removed from the underlying substrate. A free-electron metal is then indiscriminately deposited onto the original substrate and the photoresist material which remains after developing. A liftoff procedure removes the metal-coated photoresist and leaves the metal-coated substrate. Compared to photolithography, the benefit of EBL is a reduced $\lambda/2$ diffraction limit: the minimum feature-size resolution achievable using basic, visible-light photolithography is ~ 200 nm whereas that of EBL is ~ 10 nm.[38] Yu et al used EBL to fabricate nanohole and nanodisk arrays, and they examined the effect of geometry on SERS intensity.[39]

Brolo et al used FIB to mill nanohole arrays in a film of gold.[40] Nanohole arrays are especially interesting because they are closely associated with a SP-based phenomenon called extraordinary optical transmission (EOT) which will be discussed in section 4.1.

Reference 40 marks the discovery that nanohole arrays can be used as a substrate for SERS.

1.4 Potential and Limitations of SERS

In 1997, two groups independently reported enhancements as high as 14 or 15 orders of magnitude, and the detection of single molecules by SERS.[30,31] In addition, a SERS spectrum contains much structural information and may be used as a molecular fingerprint. Therefore, SERS spectroscopy has great potential for the simultaneous detection and identification of ultra-trace, down to single-molecule, analytes.

A lack of precision is generally viewed as the greatest obstacle to development of SERS-based analytical devices. The precision of a SERS measurement is typically around 15 to 20 % relative standard deviation,[41,42] but this has been reduced to a few % for applications in analytical chemistry.[41,43] The lack of precision stems from an inability to manage hotspots, where most of the signal is generated. Before SERS can be used for the detection and identification of ultra-trace analytes in a more routine way, better control over hotspots must be obtained. For this, continued development of nanofabrication techniques is essential.

Experimental observations peculiar to single-molecule SERS are, at present, poorly understood: changes in band position, bandwidth and relative band intensity; as well as the on-and-off nature of the signal (temporal "blinking").[32] This is another limitation, obviously; but it is also another area of great potential. Work directed toward understanding these observations will no doubt lead to a deeper understanding of the basic physics and chemistry which govern the behaviour of individual molecules, metal-molecule interactions, and related spectroscopic effects.

1.5 Thesis Overview

In the following chapters, we document the exploration of progressively more ordered SERS substrates.

We begin with a look at SERS from polystyrene on gold clusters (a very simple substrate). We examine the relationships that exist between sample preparation parameters, gold-cluster morphology, and SERS intensity. We assign vibrations to all bands between 250 and 1750 cm^{-1} in the ordinary Raman and SERS spectra of polystyrene by reviewing the literature, using spectral data acquired during this study, and using density functional theory (DFT) calculations performed on the styrene monomer. The correct assignment of these bands would be a significant achievement because they have been controversial in the literature for ~ 30 years. We then use our spectra, our band assignments and the SERS selection rule to determine the orientation of polystyrene's phenyl ring, relative to the surface of the gold, in our samples. It has been suggested that reactions involving silver catalyze polystyrene degradation during SERS, however we propose that heating of the substrate is sufficient to cause uncatalyzed degradation.

We then move to scratched gold films, and explore the interesting polarization effects that arise from the unidirectional features of a scratch. We introduce a method with which to quantify the extent of an observed polarization effect. We show that polarization effects can be used to selectively remove solution-phase interference signals from the SERS spectrum of an adsorbed analyte, and following proof of concept, we use our technique to monitor the electrochemically-driven desorption and readsorption of cysteine. This work is reproduced in part from a *Plasmonics* publication.[44]

Finally, we investigate the effect of geometrical parameters on SERS intensity for precisely milled nanostructures: nanohole arrays in a copper film and nanoscale gratings in a gold film. Little work has been done on subwavelength hole arrays in copper, and we document the effect of hole-periodicity on SERS intensity for nanohole arrays in this metal. The chapter on nanohole arrays in copper is reproduced in part from a *J. Phys. Chem. C* publication.[45] Much work has been done on sinusoidally-structured reflection gratings, but few publications address comb-structured transmission gratings. We report the effect of groove/line width on SERS intensity for comb-structured transmission gratings in a gold film.

1.6 References and Notes

1. Smekal A **1923** Zur Quantentheorie der Dispersion *Naturwiss.* 11, 873-875
2. Raman CV, Krishnan KS **1928** A New Type of Secondary Radiation *Nature* 121, 3048, 501-502
3. Cabannes J **1928** *Compt. Rend.* 186, 1201
4. Rocard Y **1928** *Compt. Rend.* 186, 1107
5. Long DA **1977** *Raman Spectroscopy* McGraw-Hill Inc, London
6. Ferraro JR, Nakamoto K **1994** *Introductory Raman Spectroscopy* Academic Press, London
7. Strahle WC **1993** *Combustion Science & Technology: Vol. 1, An Introduction to Combustion* p. 138-139 CRC Press, Amsterdam
8. Fleischmann M, Hendra PJ, McQuillan AJ **1974** Raman Spectra of Pyridine Adsorbed at a Silver Electrode *Chem. Phys. Lett.* 26, 2, 163-166
9. Jeanmaire DL, Van Duyne RP **1977** Surface Raman Spectroelectrochemistry Part I. Heterocyclic, Aromatic, and Aliphatic Amines Adsorbed on the Anodized Silver Electrode *J. Electroanal. Chem.* 84, 1-20
10. Albrecht MG, Creighton JA **1977** Anomalously Intense Raman Spectra of Pyridine at a Silver Electrode *J. Am. Chem. Soc.* 99, 5215-5217

11. Moskovits M **1985** Surface-Enhanced Spectroscopy *Rev. Mod. Phys.* 57, 3, 783-826

12. Aroca R **2006** *Surface-Enhanced Vibrational Spectroscopy* John Wiley & Sons Ltd, Chichester

13. Kneipp K, Moskovits M, Kneipp H, eds. **2006** *Topics in Applied Physics: Vol. 103, Surface-Enhanced Raman Scattering Physics and Applications* Springer-Verlag, Berlin Heidelberg

14. Campion A, Kambhampati P **1998** Surface-Enhanced Raman Scattering *Chem. Soc. Rev.* 27, 241-250

15. Otto A, Mrozek I, Grabhorn H, Akemann W **1992** Surface-Enhanced Raman Scattering *J. Phys. Condens. Matter* 4, 1143-1212

16. Barnes WL, Dereux A, Ebbesen TW **2003** Surface Plasmon Subwavelength Optics *Nature* 424, 824-830

17. Raether H **1988** *Surface Plasmons on Smooth and Rough Surfaces and on Gratings* Springer-Verlag, Berlin

18. Moskovits M, Suh JS **1984** Surface Selection Rules for Surface-Enhanced Raman Spectroscopy: Calculations and Application to the Surface-Enhanced Raman Spectrum of Phthalazine on Silver *J. Phys. Chem.* 88, 5526-5530

19. Dignam MJ, Moskovits M **1973** Influence of Surface Roughness on the Transmission and Reflectance Spectra of Adsorbed Species *J. Chem. Soc. Faraday Trans. 2* 69, 65-78

20. Liao PF, Wokaun A **1982** Lightning Rod Effect in Surface Enhanced Raman Scattering *J. Chem. Phys.* 76, 1, 751-752

21. Xu H, Aizpurua J, Käll M, Apell P **2000** Electromagnetic Contributions to Single-Molecule Sensitivity in Surface-Enhanced Raman Scattering *Phys. Rev. E* 62, 3, 4318-4324

22. Xu H, Käll M **2003** Polarization-Dependent Surface-Enhanced Raman Spectroscopy of Isolated Silver Nanoaggregates *ChemPhysChem* 4, 1001-1005

23. Clark RJH, Hester RE, eds. **1988** *Advances in Spectroscopy: Vol. 16, Spectroscopy of Surfaces* p. 37-89 John Wiley & Sons, Chichester

24. Lewis IR, Edwards HGM, eds. **2001** *Practical Spectroscopy: Vol. 28, Handbook of Raman Spectroscopy: From the Research Laboratory to the Process Line* CRC Press, New York
25. Wu D-Y, Li J-F, Ren B, Tian Z-Q **2008** Electrochemical Surface-Enhanced Raman Spectroscopy of Nanostructures *Chem. Soc. Rev.* 37, 1025-1041
26. Brown RJC, Milton MJT **2008** Nanostructures and Nanostructured Substrates for Surface-Enhanced Raman Scattering (SERS) *J. Raman Spectrosc.* 39, 1313-1326
27. Aroca R, Jennings C, Kovacs GJ, Loutfy RO, Vincett PS **1985** Surface-Enhanced Raman Scattering of Langmuir-Blodgett Monolayers of Phthalocyanine by Indium and Silver Island Films *J. Phys. Chem.* 89, 4051-4054
28. Kovacs GJ, Loutfy RO, Vincett PS, Jennings C, Aroca R **1986** Distance Dependence of SERS Enhancement Factor from Langmuir-Blodgett Monolayers on Metal Island Films: Evidence for the Electromagnetic Mechanism *Langmuir* 2, 689-694
29. Stöckle RM, Deckert V, Fokas C, Zenobi R **2000** Controlled Formation of Isolated Silver Islands for Surface-Enhanced Raman Scattering *Appl. Spectrosc.* 54, 11, 1577-1583
30. Kneipp K, Wang Y, Kneipp H, Perelman LT, Itzkan I, Dasari RR, Feld MS **1997** Single Molecule Detection Using Surface-Enhanced Raman Scattering (SERS) *Phys. Rev. Lett.* 78, 9, 1667-1670
31. Nie S, Emory SR **1997** Probing Single Molecules and Single Nanoparticles by Surface-Enhanced Raman Scattering *Science* 275, 1102-1106
32. Pieczonka NPW, Aroca RF **2008** Single Molecule Analysis by Surface-Enhanced Raman Scattering *Chem. Soc. Rev.* 37, 946-954
33. Vlčková B, Moskovits M, Pavel I, Šišková K, Sládková M, Šlouf M **2008** Single-Molecule Surface-Enhanced Raman Spectroscopy from a Molecularly-Bridged Silver Nanoparticle Dimer *Chem. Phys. Lett.* 455, 131-134
34. Baker GA, Moore DS **2005** Progress in Plasmonic Engineering of Surface-Enhanced Raman-Scattering Substrates Toward Ultra-Trace Analysis *Anal. Bioanal. Chem.* 382, 1751-1770

35. Willets KA, Van Duyne RP **2007** Localized Surface Plasmon Resonance Spectroscopy and Sensing *Annu. Rev. Phys. Chem.* 58, 267-297

36. Stuart DA, Yonzon CR, Zhang X, Lyandres O, Shah NC, Glucksberg MR, Walsh JT, Van Duyne RP **2005** Glucose Sensing Using Near-Infrared Surface-Enhanced Raman Spectroscopy: Gold Surfaces, 10-Day Stability, and Improved Accuracy *Anal. Chem.* 77, 13, 4013-4019

37. Zhang X, Young MA, Lyandres O, Van Duyne RP **2005** Rapid Detection of an Anthrax Biomarker by Surface-Enhanced Raman Spectroscopy *J. Am. Chem. Soc.* 127, 4484-4489

38. Chen Y, Pépin A **2001** Nanofabrication: Conventional and Nonconventional Methods *Electrophoresis* 22, 187-207

39. Yu Q, Guan P, Qin D, Golden G, Wallace PM **2008** Inverted Size-Dependence of Surface-Enhanced Raman Scattering on Gold Nanohole and Nanodisk Arrays *Nano Lett.* 8, 7, 1923-1928

40. Brolo AG, Arctander E, Gordon R, Leathem B, Kavanagh KL **2004** Nanohole-Enhanced Raman Scattering *Nano Lett.* 4, 2015-2018

41. Laserna JJ **1993** Combining Fingerprinting Capability with Trace Analytical Detection: Surface-Enhanced Raman Spectrometry *Anal. Chim. Acta* 283, 607-622

42. Kneipp K, Kneipp H, Itzkan I, Dasari RR, Feld MS **1999** Ultrasensitive Chemical Analysis by Raman Spectroscopy *Chem. Rev.* 99, 2957-2975

43. Bell SEJ, Sirimuthu NMS **2008** Quantitative Surface-Enhanced Raman Spectroscopy *Chem. Soc. Rev.* 37, 1012-1024

44. Anema JR, Brolo AG **2007** The Use of Polarization-Dependent SERS from Scratched Gold Films to Selectively Eliminate Solution-Phase Interference *Plasmonics* 2, 157-162

45. Anema JR, Brolo AG, Marthandam P, Gordon R **2008** Enhanced Raman Scattering from Nanoholes in a Copper Film *J. Phys. Chem. C* 112, 17051-17055

Chapter 2: Polystyrene on Gold Clusters

2.1 Introduction

In this chapter, we explore SERS from polystyrene samples prepared in a novel way: by alternating vapour deposition of gold with plasma-induced polymerization of styrene gas. During each vapour deposition step, a series of gold clusters are produced. The gold clusters form a very simple (highly disordered) SERS substrate - in essence, a sparse island film. We examine the relationships that exist between sample preparation parameters, gold-cluster morphology, and SERS intensity.

The ideal size of a single noble-metal particle for excitation of SPs with visible light is between 10 and 100 nm.[1,2] As two particles approach, the electromagnetic fieldstrength between them will increase dramatically.[1,3,4] When their distance becomes sufficiently small, SERS originating from the interstice will become more intense than the SERS that originated from the isolated particles.[1,4] For example, Käll et al were able to detect single hemoglobin molecules between silver particles (spaced somewhere between 1 and 5.5 nm apart), but they were not able to detect single hemoglobin molecules on individual silver particles.[5] Our results are consistent with the effect of particle size and spacing on SERS intensity just described.[6]

The effect of deposition rate on morphology during formation of a silver island film on a glass substrate is known: slower deposition rates yield islands that are well separated and have higher topographical features whereas faster deposition rates yield islands that are more spread out over the surface.[7-10] This relationship between deposition rate and morphology was observed again in the present work for a gold film deposited onto polystyrene.

In addition, the effect of deposition rate on SERS intensity has been studied for the silver-on-glass system using 458 and 514 nm excitation wavelengths: slower deposition rates produce the kinds of structures that give the best SERS.[8,9] We found the opposite is true for gold-on-polystyrene when a 633 nm excitation wavelength is used: faster deposition rates produce the kinds of structures that give the best SERS.

SERS from island films in contact with polystyrene has proven useful in the study of diffusion and surface segregation. To obtain the self-diffusion coefficient of polystyrene, Boerio et al[11] coated a silver island film with polystyrene and then deuterated polystyrene. The polystyrene film was thick enough that the deuterated polystyrene lay outside the SP field, and only SERS from polystyrene was seen initially. As the sample was heated, the SERS signal from deuterated polystyrene grew in. The thickness of the polystyrene film and the time required to reach equilibrium were used to calculate the self-diffusion coefficient. In addition, Boerio et al[12,13] used SERS from silver island film overlayers to study the surface enrichment of deuterated polystyrene that occurs when blends of polystyrene and deuterated polystyrene are heated. This enrichment occurs because deuterated polystyrene has a slightly lower surface free energy than polystyrene.

There are some practical reasons for continued study of the SERS of polystyrene; we discuss three of them in the following paragraphs.

Polystyrene nanospheres have been used to improve the light-extraction efficiency of thin-film phosphors.[14] They have also been used in the fabrication of nanostructured surfaces for sensor[15] and magnet[16] applications. In each of these references (14 to 16), sphere-packing quality is of great consequence. Djaoued et al have recently shown that when small gold particles (5 or 20 nm) are mixed with larger polystyrene spheres (510 nm), SERS obtained from the polystyrene may be used to evaluate packing quality and examine packing defects.[17]

Since polystyrene is a widely used compound of great industrial importance, understanding its photochemical[18,19] and thermal[20] degradation is important. Polystyrene has no absorption bands in the visible region of the spectrum,[21] therefore SERS cannot directly contribute to an understanding of its photodecomposition. However SERS may contribute to an understanding of its thermal decomposition,[22] especially if the metallic SERS substrate does not alter the usual mechanistic pathway by participating chemically in the degradation process. It has been suggested that reactions involving silver catalyze polystyrene degradation during SERS;[22,23] but our SERS substrates, which are composed of unreactive gold, yield no fewer decomposition peaks than SERS substrates composed of silver.[22,23] Thus we provide evidence that silver substrates do not participate, chemically, in the degradation process.

Band assignments provide the foundation for understanding spectroscopic data. Many authors[11,22,24-29] have assigned vibrations to the bands in the ordinary Raman spectrum of polystyrene using Wilson's notation.[26,30] Some of their assignments are contradictory, however, and we have found only one publication[11] where assignments have been made for the SERS spectrum. Clearly, more work is needed in this area. In the present study, we assign bands in the ordinary Raman and SERS spectra of polystyrene by reviewing the literature and by examining spectroscopic data and density functional theory (DFT) results. We then use our assignments to determine the orientation of polystyrene's phenyl ring relative to the surface of our gold clusters.

For clarity, we now summarize the contributions made in this chapter. We show that SERS may be obtained from polystyrene samples created in a novel way: by alternating vapour deposition of gold with plasma-induced polymerization of styrene gas. We examine the relationships that exist between vapour deposition rate, gold-cluster size and spacing, and SERS intensity. Using Wilson's notation, we assign vibrations to all bands between 250 and 1750 cm^{-1} in the ordinary Raman and SERS spectra of polystyrene. We determine the orientation of polystyrene's phenyl ring relative to the surface of the gold. It has been suggested that reactions involving silver catalyze polystyrene degradation during SERS; however, we contend that silver is not necessary for the degradation to occur.

2.2 Experimental Methods

2.2.1 Preparation of the Polystyrene/Gold-Cluster Samples

Polystyrene/gold-cluster samples were prepared by our collaborators Alexandre Felten (University of Namur, Belgium) and Carla Bittencourt (University of Mons-Hainaut, Belgium).

Each sample was prepared by cleaning a piece of silicon (Si) wafer with methanol, then placing it in a vacuum chamber made for the application of inductively coupled plasmas[31] and modified to permit vapour deposition of metals as well.

This chamber was pumped down to 0.08 Torr. Styrene was introduced into the chamber as a gas and polymerized by radicals in an 80 W, 13.56 MHz plasma for 1 min 30 s. Polystyrene prepared in this way adhered to the silicon wafer.

Gold was added by high-temperature evaporation. In this chapter, we will focus on two samples: a "low current" one and a "high current" one. Gold was added to the low current sample by passing 77.3 mA through a gold rod for 30 s. The high current sample was prepared in the same way, except 83.3 mA were used.

Both samples were prepared by alternating polymerization of styrene with either low current or high current deposition of gold: three layers of each, beginning with polymerization.

2.2.2 Spectroscopy

SERS spectra were obtained from the polystyrene/gold-cluster samples described above. A 35 mW He-Ne laser (Melles Griot) was used to provide light with a wavelength of 632.8 nm. The angle between light incident upon a sample and scattered light collected from the sample was 90 degrees. The scattered light passed through a Kaiser super-notch filter, was directed into a Kaiser Holospec *f*/1.4 spectrograph, and was detected by an Andor DV-401-BV CCD. Spectral resolution was ~ 3 cm^{-1}. Cosmic rays were removed, and SERS spectra were baseline-corrected.

Ordinary Raman spectra were obtained from solid polystyrene powder on a glass microscope slide. These spectra were acquired at a later date, after a light microscope was incorporated into our optical system. The (backscattering geometry) experimental setup used is illustrated and described in section 4.2.4. Spectral resolution was ~ 3 cm^{-1}. Ordinary Raman spectra were baseline-corrected.

Peak intensities obtained from polystyrene/gold-cluster and polystyrene powder samples are not directly comparable. The experimentally observed scattering intensity is dependent upon, for example, density of polystyrene in the laser spot; and this is expected to vary dramatically between the two sample types. It is therefore inconsequential that different experimental setups were used to collect SERS and ordinary Raman spectra. To correct for sample and setup differences, all peak intensities were normalized using the ν_{12} intensity; and these normalized values were compared to obtain the relative enhancement values in Table 2.1 (see section 2.3.2). The ν_{12} band was an arbitrary choice, but it worked well (most of the relative enhancement values in Table 2.1 are > 1).

In this chapter, SERS intensity is called "weak" when the signal to noise ratio (S/N) is < 10. SERS intensity is called "intermediate" when 10 < S/N < 30, and "strong" when S/N is > 30.

2.2.3 DFT Calculations

DFT calculations were performed using B3LYP/6-311G/restricted in Gaussian 03W, Version 6.0.[32]

2.3 Results and Discussion

2.3.1 Sample Preparation Parameters, Gold-Cluster Morphology, and SERS Intensity

In Figure 2.1 we present SERS spectra and an SEM image acquired from the low current sample (gold was evaporated using 77.3 mA for 30 s/layer). When a survey of this sample was made, one area was found to have intermediate (Figure 2.1a and Figure 2.1b, red curves) SERS activity and four areas were found to have weak (Figure 2.1a and Figure 2.1b, blue curves) or no SERS activity. Cosmic rays were removed, and the spectra shown in Figure 2.1a and Figure 2.1b were baseline-corrected; raw spectra appear in Appendix A.

The cluster shown in Figure 2.1c was found in the same region of the low current sample used to obtain the intermediate-intensity SERS spectrum. It is about 1000 nm in diameter, too large to yield very strong SERS. The cluster is not smooth, however, and smaller features on its surface are expected to have some SERS activity. Clusters found in regions that showed no SERS were similar to those found in the region from which an intermediate SERS spectrum was obtained, but far fewer of them were present.

In Figure 2.2 we present SERS spectra and an SEM image acquired from the high current sample (gold was evaporated using 83.3 mA for 30 s/layer). When a survey of this sample was made, all six positions tested gave strong (Figure 2.2a, red curve) or intermediate (Figure 2.2a, blue curve) SERS intensity. Cosmic rays were removed, and the spectra shown in Figure 2.2a were baseline-corrected; raw spectra appear in Appendix A.

Figure 2.2b shows an SEM image obtained from the high current sample. Many of the clusters shown here are in the ideal size range for SERS: 10 to 100 nm.[1,2] Moreover, the shape and the graininess of the larger clusters would seem to indicate that they are actually aggregates of the smaller sized ones. As explained in section 2.1, extraordinarily high electromagnetic fields exist in the space between structures, and a molecule situated in this type of interstice will yield very strong SERS.[1,3-5]

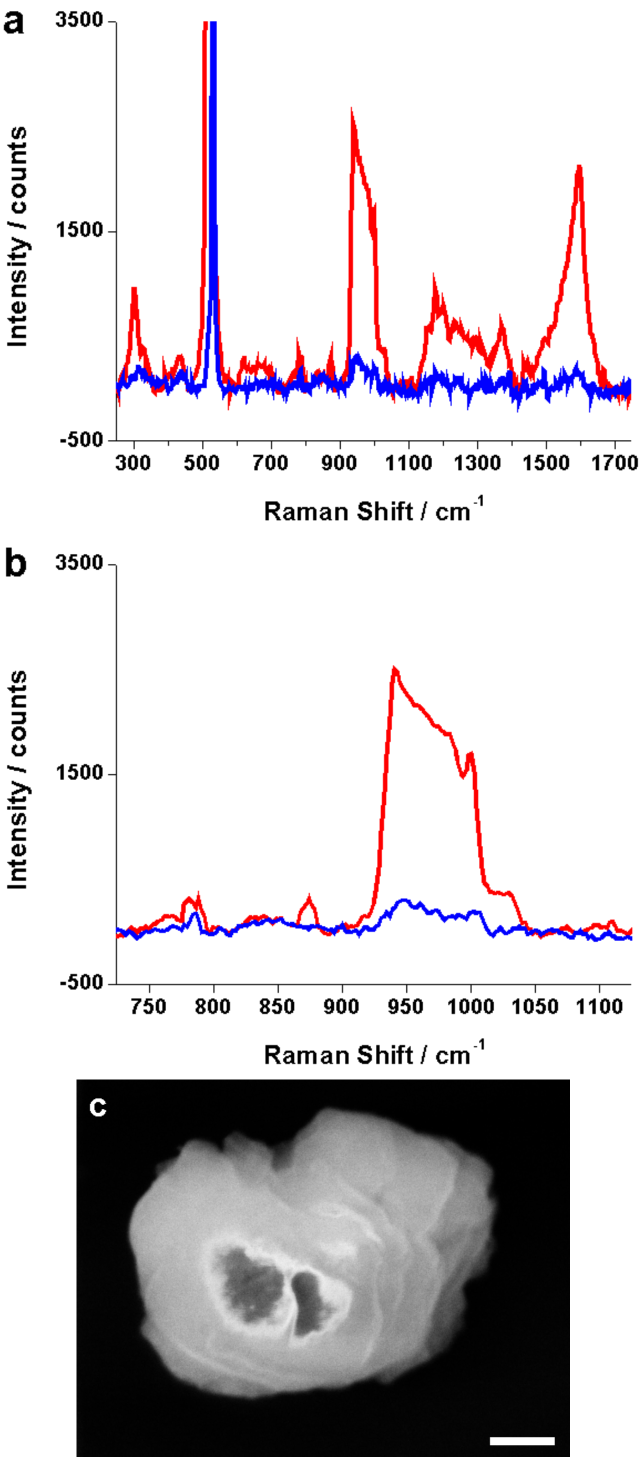

Figure 2.1 (a) Spectra showing intermediate (red curve) and weak (blue curve) SERS obtained from the low current sample: gold was evaporated using 77.3 mA for 30 s/layer. Acquisition time for both spectra was 600 s. (b) Expansion of the 750 to 1100 cm^{-1} region showing the ν_{12} peak at 999 cm^{-1} beside the broad silicon band that ranges from about 930 to 990 cm^{-1}. (c) SEM image of the area that gave the intermediate SERS spectrum. Magnification is 100k × and the length of the scale bar is 200 nm.

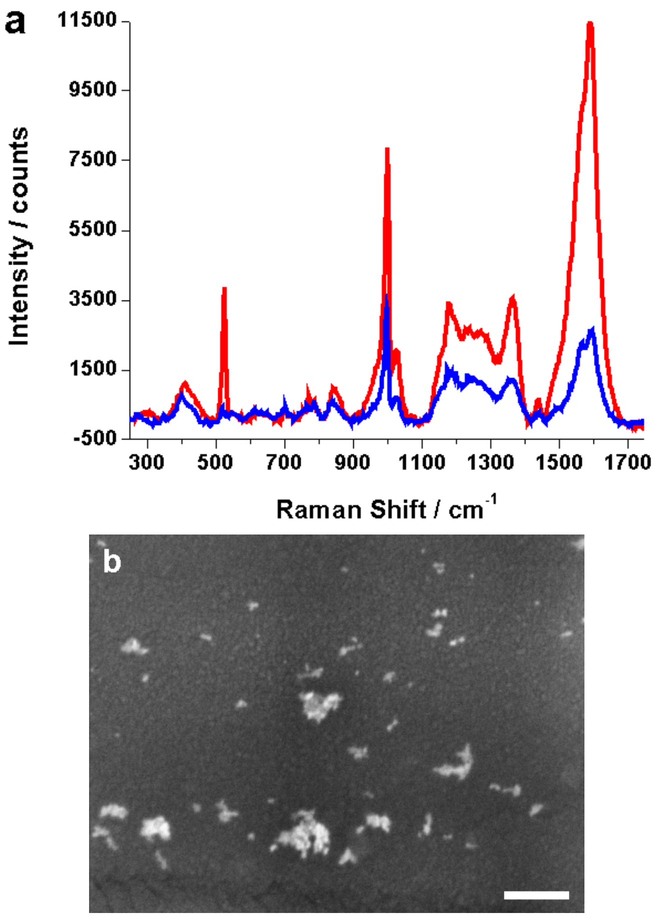

Figure 2.2 (a) Spectra showing strong (red curve, acquisition time was 300 s) and intermediate (blue curve, acquisition time was 600 s) SERS obtained from the high current sample: gold was evaporated using 83.3 mA for 30 s/layer. Acquisition time was shortened for the spectrum showing strong SERS to prevent saturation of the detector and flat-topping of the most intense peaks. (b) SEM image of the area that gave the strong SERS spectrum. Magnification is 100k × and the length of the scale bar is 200 nm.

The SEM images show that gold clusters were larger and more diffuse in the low current sample (Figure 2.1c) than in the high current sample (Figure 2.2b). This observation is consistent with previously published results concerning the effect of evaporation rate on the morphology of silver island films deposited onto glass: slower deposition rates yield islands that are well separated and have higher topographical features whereas faster deposition rates yield islands that are more spread out over the surface.[7-10]

As explained above, the relationship observed between evaporation rate and SERS-substrate morphology, and the one observed between SERS-substrate morphology and SERS intensity, are both consistent with the literature. The relationship that we observed between evaporation rate and SERS intensity, however, is not consistent with the literature. It is our high current sample, rather than our low current one, that displayed stronger SERS. This is contrary to results published by Cotton et al[8] and Rowlen et al[9] regarding the effect of deposition rate on SERS intensity for silver island films on glass using 458 and 514 nm excitation. In their experiments, lower deposition rates yielded stronger SERS.[8,9]

We point out that these excitation wavelengths are shorter than the one we used; and both authors indicate that, for silver island films on glass, the inverse relationship between deposition rate and SERS intensity is weakened at longer excitation wavelengths.[8,9] In fact, Figure 2 in reference 8 suggests that for excitation wavelengths above ~ 685 nm, the relationship becomes proportional rather than inverse. This is a consequence of the way in which the film's optical density profile depends on island size, shape, and packing.[8]

In addition, system-specific properties like surface free energy and surface morphology affect adatom mobility and the metal crystallization process. An understanding of how all such properties differ between silver on glass and gold on our polystyrene surfaces would be necessary to explain why a higher deposition rate, rather than a lower one, gave a more effective SERS substrate and therefore stronger SERS in our case. Such investigation lies beyond the scope of this work.

We conclude that when styrene polymerization is alternated with 30s of gold deposition, 83.3 mA are more suitable than 77.3 mA for acquisition of a SERS spectrum of the polymer matrix using a 633 nm excitation source. We note that since deposition time was held constant at 30 s, a greater quantity of gold was deposited on the high current sample. This likely also contributes to the strong SERS intensity obtained from the high current sample, as more gold should mean a greater surface area interacting with polystyrene.

2.3.2 Band Assignments

Figure 2.3 shows the ordinary Raman spectrum of solid polystyrene powder.

Spectroscopic results and conclusions are amassed in Table 2.1. Experimental band positions, from ordinary Raman and SERS spectra of polystyrene, are listed in columns 1 and 2 respectively. The relative enhancement values in column 3 were obtained by dividing ν_{12}-normalized SERS intensity by ν_{12}-normalized ordinary Raman intensity for each peak. The numbers in column 3 indicate how many times the intensity of a Raman peak is enhanced by the surface when the ν_{12} peak is used as a reference. Vibrational modes and their ordinary Raman band positions, calculated for the styrene monomer using DFT, are listed in column 4. The % difference between each styrene DFT position (column 4) and polystyrene experimental position (column 1) is also provided in column 4. Peak assignments and symmetry information are given in column 5. Peak assignments were made by comparing five types of data: ordinary Raman in the literature,[11,22,24-29] SERS in the literature,[11,22] ordinary Raman data acquired during this study (3 spectra), SERS data acquired during this study (8 spectra), and ordinary Raman data obtained for the styrene monomer using DFT.

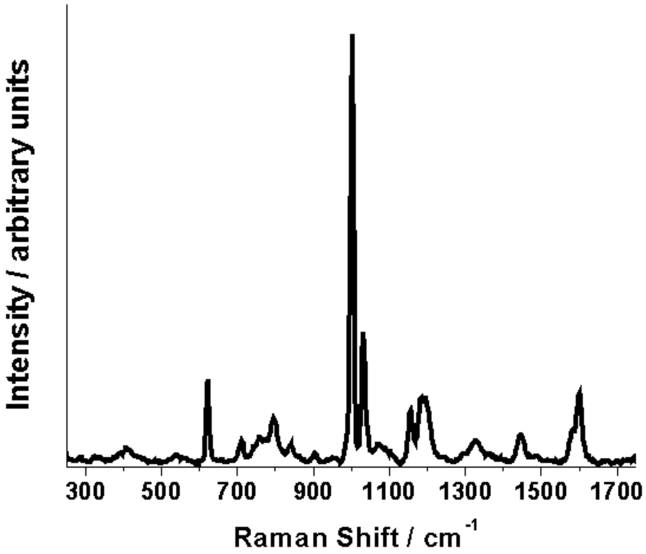

Figure 2.3 The ordinary Raman spectrum of solid polystyrene powder. Acquisition time was 270 s.

We note that the sharp SERS band at 517 cm^{-1} (Figure 2.1a and Figure 2.2a) and the broad SERS band ranging from 930 to 990 cm^{-1} (Figure 2.1a and Figure 2.1b) are due to the silicon substrate. This was determined by running a silicon blank.

Many authors[11,22,24-29] have assigned vibrations to the bands in the ordinary Raman spectrum of polystyrene, and our ordinary Raman assignments were made by comparing the results presented in this reasonably large body of work. DFT calculations, performed on the styrene monomer, were then used to confirm our literature-based ordinary Raman assignments. Previous to the current work, only one publication[11] has attempted thorough and systematic assignment of all bands in the SERS spectrum. We used ordinary Raman band positions, as well as reference 11, to make our SERS assignments. Although some peak shifting (compared to the ordinary Raman position) does occur in the SERS, many SERS assignments were straightforward when made in this way. Other assignments were less straightforward; hence treatment of the polystyrene band at 543

cm^{-1} (ordinary Raman position), as well the bands at 1442, 1249, 1183 and 770 cm^{-1} (SERS positions), is justified below.

In all SERS spectra but one (Figure 2.2a blue curve), the 543 cm^{-1} band in the ordinary Raman spectrum of polystyrene was hidden or obscured by the strong silicon peak at 517 cm^{-1}. Since the position and the relative enhancement could not be averaged, SERS data for this band was left absent from Table 2.1. DFT calculations performed on the styrene monomer show an in-plane ring-to-vinyl bending/rocking band at 575 cm^{-1} (there is a 6 % difference between 543 and 575 cm^{-1}). Presumably, an analogous motion occurs between the ring and the backbone in the polymer. Our assignment is in agreement with that of Sears, Hunt and Stevens.[27]

From Figure 2.1, Figure 2.2 and Table 2.1, it may be seen that in general the largest peaks (305 in some spectra, 1183, 1249, 1368, 1567, 1594 cm^{-1}) and the greatest relative enhancements (305, 425, 845, 1567, 1594 cm^{-1}) occur where chain modes or degradation products (including graphite) are involved. Since the band at 1442 cm^{-1} is weak and has a modest relative enhancement, it is probably due to the 19b ring mode[26-28] rather than the δCH_2 chain mode[11,26,28] or some degradation product[22]. Our DFT calculations confirm a 19b contribution, but they cannot be used to rule out a δCH_2 contribution (chain modes cannot appear in our DFT results because only the styrene monomer was modeled). Thus, although we believe δCH_2 does not contribute to the band at 1442 cm^{-1}, we cannot discount the possibility of a contribution from this mode. Therefore both 19b and δCH_2 are given in the band assignments column of Table 2.1.

Table 2.1 Ordinary Raman and SERS spectra, obtained experimentally for polystyrene, are compared in columns 1 to 3. Vibrational modes and their ordinary Raman band positions, calculated for the styrene monomer using DFT, are listed in column 4. The % difference between each styrene DFT position (column 4) and polystyrene experimental position (column 1) is also provided in column 4. Band assignments, with symmetry information, are given in column 5. References 24 to 29 give ordinary Raman data only. References 11 and 22 give both ordinary Raman and SERS data.

Ordinary Raman Position, cm^{-1}	SERS Position, cm^{-1}	Relative Enhance-ment	DFT Position, cm^{-1}, with % Difference	Assignment with Symmetry and References
	305			C-C-C [25,26,28]
407	425	6.7	16a @ 420 (3%)	16a A_2 α_{xy} [25-28] and C-C-C [25,28]
543	under Si		in-plane ring-to-vinyl bending/rocking @ 575 (6%)	in-plane ring-to-chain bending/rocking [27]
623	622	0.75	6b @ 652 (4%)	6b B_2 α_{yz} [11,26-29]
711	677	3.5	4 @ 667 (-7%)	4 B_1 α_{xz} [26,27,29]
761			11 @ 724 (-5%)	11 B_1 α_{xz} [26,27,29]
796	770	1.8	1 @ 795 (0%)	1 A_1 $\alpha_{xx}\alpha_{yy}\alpha_{zz}$ [26,27,29]
841	845	5.7	10a @ 871 (3%)	10a A_2 α_{xy} [11,26,27,29] and γCH_2 [11,26]
904			17b @ 951 (5%)	17b B_1 α_{xz} [11,26-28]
1002	999	1.0 (reference)	12 @ 1026 (2%)	12 A_1 $\alpha_{xx}\alpha_{yy}\alpha_{zz}$ [26,27]
1032	1026	0.86	18a @ 1054 (2%)	18a A_1 $\alpha_{xx}\alpha_{yy}\alpha_{zz}$ [11,26-28]
1073			18b @ 1124 (5%)	18b B_2 α_{yz} [26-28]
1156			15 @ 1212 (5%)	15 B_2 α_{yz} [11,26-28]
1183	1183	3.7	9a @ 1230 (4%)	Ordinary Raman: 9a A_1 $\alpha_{xx}\alpha_{yy}\alpha_{zz}$ [11,26,27] SERS: 15, 9a, 13 and/or degradation product [22]
1196			13 @ 1242 (4%)	13 A_1 $\alpha_{xx}\alpha_{yy}\alpha_{zz}$ [11,26,27]
	1249			degradation product [22]
1326			14 @ 1367 (3%)	14 B_2 α_{yz} [26,28]
	1368			graphite [11,24]
1448	1442	1.8	19b @ 1481 (2%)	19b B_2 α_{yz} [26-28] and maybe δCH_2 [11,26,28]
1583	1567	13	8b @ 1618 (2%)	Ordinary Raman: 8b B_2 α_{yz} [11,26,27] SERS: 8b and graphite [11,24]
1600	1594	7.8	8a @ 1644 (3%)	Ordinary Raman: 8a A_1 $\alpha_{xx}\alpha_{yy}\alpha_{zz}$ [11,26,27] SERS: 8a and graphite [11,24]

Since there are no ordinary Raman bands in the vicinity of 1249 cm^{-1}, we assigned this SERS peak to a degradation product in agreement with reference 22.

The SERS band at 1183 cm^{-1} was also assigned to a degradation product in reference 22. Indeed its high intensity in our spectra is typical of a degradation product band. Moreover, we observed that it is always seen in combination with the band at 1249 cm^{-1} (either both are present or both are absent), and the intensity ratio between the two is fairly constant at 1.3 to 1. Since the peak at 1249 cm^{-1} has been assigned to a degradation product, this relationship between the two suggests that they are due either to the same degradation product or to degradation products which form together during laser irradiation.

On the other hand, it seems unreasonable to assume that none of ν_{15}, ν_{9a} and ν_{13} contribute to the 1183 cm^{-1} band. Although intensity of the 1183 cm^{-1} band is high enough to be consistent with other degradation product bands, a moderate relative enhancement of 3.7 is obtained by using an average of the ν_{15}, ν_{9a} and ν_{13} ordinary Raman peak intensities. We therefore concede that the SERS band at 1183 cm^{-1} is difficult to assign, but we believe some combination of ν_{15}, ν_{9a}, ν_{13} and degradation products - rather than just one of these - are responsible for the peak.

The SERS band at 770 cm^{-1} may be assigned as ν_{11} (upshifted 9 cm^{-1}, with a relative enhancement of 3.2 for this B_1 mode) or ν_1 (downshifted 26 cm^{-1}, with a relative enhancement of 1.8 for this A_1 mode). While B_1 modes contain α_{xz}, A_1 modes contain $\alpha_{xx}\alpha_{yy}\alpha_{zz}$ and should be enhanced in the SERS no matter what the orientation of the molecule on the surface. It is therefore more likely that the weaker ν_{11} (B_1, α_{xz}) mode would disappear in the SERS than the stronger ν_1 (A_1, $\alpha_{xx}\alpha_{yy}\alpha_{zz}$) mode, and we assign the SERS peak at 770 cm^{-1} to ν_1.

It is worth noting that the ν_{6b} and ν_{18a} are suppressed, rather than enhanced, in the SERS. This may be an artifact of using ν_{12} as a reference when calculating relative enhancements; i.e., if any band is enhanced to a lesser extent than the ν_{12} band, its relative enhancement will be less than 1. Or the suppression may be real, as suppression was reported by Boerio et al[11] for ν_{6b} and ν_{15}, and is therefore not without precedent. Further, some peaks disappear completely in the SERS, both in this work and in reference 11. We believe that suppression of ν_{6b} is real because it is strong (25 %) and because it is corroborated by Boerio et al.[11] Suppression of ν_{18a} is probably an artifact; the suppression here is weaker, and suppression of an A_1 mode is unlikely.

2.3.3 Orientation of Polystyrene's Phenyl Ring Relative to the Gold

When analyzing polystyrene phenyl ring modes, the chain can be neglected and the local symmetry of the ring can be used.[26] Since monosubstituted benzenes have C_{2v} symmetry, polystyrene's phenyl ring belongs to this point group as well. The x-, y-, and z-axes are defined as shown in Figure 2.4.[26,33]

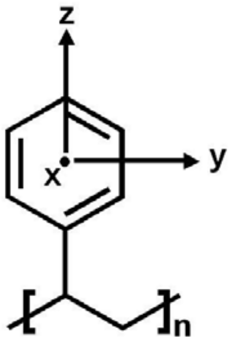

Figure 2.4 The x-, y-, and z-axes are defined for polystyrene's phenyl ring.

In general, a band is strongly enhanced in the SERS if the associated mode's polarizability change is perpendicular to the surface of the metal.[34] If polystyrene's phenyl ring were to approach the surface of the gold face-on, out-of-plane modes (those which contain an x-component) should be most enhanced. If the ring were to approach the gold edge-on, in-plane modes should be most enhanced (z-component modes enhanced if head-on, y-component modes enhanced if side-on). Of course, face-on is the only orientation for which chemisorption is possible; only physisorption is possible for edge-on orientations.

The symmetries and relative enhancements given in Table 2.1 may therefore be used to examine the orientation of polystyrene's phenyl ring relative to the gold. However, we must first distinguish between bands that can provide useful information about the orientation and bands that cannot. As stated previously, A_1 modes contain $\alpha_{xx}\alpha_{yy}\alpha_{zz}$ and should be enhanced in the SERS no matter what the orientation of the molecule on the surface. Bands assigned to modes with A_1 symmetry, therefore, provide little or no useful information about orientation. Bands which have some contribution from chain modes, degradation products or silicon provide no useful information; here the extent of ring mode enhancement is unknown.

If we disregard all bands which are not useful for finding the orientation of the phenyl ring relative to the metal, we are left with the following modes: ν_{6b}, ν_4, ν_{11}, ν_{17b}, ν_{18b} and ν_{19b} (if δCH_2 does not contribute to the ν_{19b} band). We have left ν_{14} out of this list because we do not know if the ν_{14} band disappears in the SERS or if it is just buried beneath the degradation product band at 1249 cm^{-1} and/or the graphite band at 1368 cm^{-1}. Similarly, we have left ν_{15} absent because we do not know if it disappears in the SERS or if it contributes to the band at 1183 cm^{-1} (along with ν_{9a}, ν_{13} and/or a degradation product). Of the six usable modes, ν_4, ν_{11} and ν_{17b} have B_1 symmetry and ν_{6b}, ν_{18b} and ν_{19b} have B_2 symmetry. Of the B_1 modes (which transform as α_{xz}), ν_4 is enhanced but ν_{11} and ν_{17b} disappear in the SERS. Of the B_2 modes (which transform as α_{yz}), ν_{19b} is enhanced, ν_{6b} is suppressed, and ν_{18b} disappears in the SERS. Since both the usable B_1 modes and the usable B_2 modes have inconsistent enhancement, it would appear that polystyrene's phenyl ring does not lie edge-on or face-on relative to the surface of the metal, but rather lies at some angle (on average).

It is unfortunate that no A_2 modes (these transform as α_{xy}) survive the elimination of bands which provide inconclusive evidence regarding orientation. In section 2.3.2 we asserted that chain-mode (and degradation-product, including graphite) contributions are large compared to ring-mode contributions. If, on the other hand, the ν_{16a} and ν_{10a} ring contributions are significant, then perhaps the A_2 modes can be considered. Both are enhanced in the SERS, and this may indicate that although the ring is tilted, it is more face-on/side-on than head-on.

2.3.4 A Comment on the Mechanism of Polystyrene Degradation

It is widely accepted that the two peaks at approximately 1400 and 1600 cm^{-1} in the SERS spectrum of polystyrene are due to graphite. In this section, we are not interested in the two graphite peaks but in the other two degradation-product bands: those which appear at 1183 and 1249 cm^{-1} in the present work and which are less well understood.

It has been proposed that reactions involving silver catalyze polystyrene degradation during SERS.[22,23] In the current work, gold clusters were used as the substrate for SERS and degradation-product bands similar to those presented in references 22 and 23 were obtained. If our gold clusters are chemically inert, appearance of these two bands in our spectra would suggest that catalysis by silver is unnecessary and heating of the SERS substrate is sufficient to cause uncatalyzed degradation.

Now although gold nanoparticles may possess catalytic activity,[35,36] catalysis by gold is generally associated with very small gold particles (< 5 nm) and an oxide support (e.g. TiO_2, SiO_2, Al_2O_3, MgO).[35,37-39] Therefore, the gold clusters used in this work are quite probably unreactive for two reasons: they are larger[40] than 5 nm and they were deposited onto polystyrene-coated Si.

Since our gold clusters most likely possess no catalytic activity, the appearance of bands at 1183 and 1249 cm^{-1} in our SERS spectra would suggest that reactions involving silver do not play a role in the degradation mechanism when silver is present as the SERS substrate. We propose that heating of the SERS substrate (in the presence of O_2[22,23]) is sufficient to cause uncatalyzed (oxidative[22,23]) degradation.

2.4 Conclusions

Intermediate to weak (Figure 2.1a and Figure 2.1b) or no SERS was obtained from the large, well separated gold clusters (Figure 2.1c) produced by a low rate of gold deposition (77.3 mA for 30 s/layer). Strong to intermediate (Figure 2.2a) SERS was obtained from the smaller, more abundant gold clusters (Figure 2.2b, some of the larger clusters here appear to be aggregates of the smaller ones) produced by a high rate of gold deposition (83.3 mA for 30 s/layer).

Vibrational modes have been assigned to all bands between 250 and 1750 cm^{-1} in the ordinary Raman spectrum and the SERS spectrum of polystyrene (Table 2.1). These assignments, together with the SERS selection rule,[34] were used to determine that polystyrene's phenyl ring is tilted with respect to the surface of the gold in our samples.

Finally, we found that silver is not necessary for polystyrene degradation to occur during SERS.

2.5 References and Notes

1. Moskovits M **2005** Surface-Enhanced Raman Spectroscopy: A Brief Retrospective *J. Raman Spectrosc.* 36, 485-496
2. Zeman EJ, Schatz GC **1987** An Accurate Electromagnetic Theory Study of Surface Enhancement Factors for Ag, Au, Cu, Li, Na, Al, Ga, In, Zn, and Cd *J. Phys. Chem.* 91, 634-643
3. Brown RJC, Wang J, Milton MJT **2007** Electromagnetic Modelling of Raman Enhancement from Nanoscale Structures as a Means to Predict the Efficacy of SERS Substrates *J. Nanomater.* 2007, 12086
4. Xu H, Aizpurua J, Käll M, Apell P **2000** Electromagnetic Contributions to Single-Molecule Sensitivity in Surface-Enhanced Raman Scattering *Phys. Rev. E* 62, 3, 4318-4324
5. Xu H, Bjerneld EJ, Käll M, Borjesson L **1999** Spectroscopy of Single Hemoglobin Molecules by Surface Enhanced Raman Scattering *Phys. Rev. Lett.* 83, 21, 4357-4360
6. See also section 1.2.3.
7. Sennett RS, Scott GD **1950** The Structure of Evaporated Metal Films and Their Optical Properties *J. Opt. Soc. Am.* 40, 4, 203-211
8. Schlegel VL, Cotton TM **1991** Silver-Island Films as Substrates for Enhanced Raman Scattering: Effect of Deposition Rate on Intensity *Anal. Chem.* 63, 241-247
9. Semin DJ, Rowlen KL **1994** Influence of Vapor Deposition Parameters on SERS Active Ag Film Morphology and Optical Properties *Anal. Chem.* 1994, 66, 4324-4331

10. Stöckle RM, Deckert V, Fokas C, Zenobi R **2000** Controlled Formation of Isolated Silver Islands for Surface-Enhanced Raman Scattering *Appl. Spectrosc.* 54, 11, 1577-1583

11. Hong PP, Boerio FJ, Clarson SJ, Smith SD **1991** An Investigation of the Interdiffusion of Polystyrene and Deuterated Polystyrene Using Surface-Enhanced Raman Scattering *Macromolecules* 24, 4770-4776

12. Hong PP, Boerio FJ, Smith SD **1993** Surface Segregation in Blends of Polystyrene and Deuterated Polystyrene *Macromolecules* 26, 1460-1464

13. Hong PP, Boerio FJ, Smith SD **1994** Effect of Annealing Time, Film Thickness, and Molecular Weight on Surface Enrichment in Blends of Polystyrene and Deuterated Polystyrene *Macromolecules* 27, 596-605

14. Lee YK, Oh JR, Do YR **2007** Enhanced Extraction Efficiency of $Y_2O_3:Eu^{3+}$ Thin-Film Phosphors Coated with Hexagonally Close-Packed Polystyrene Nanosphere Monolayers *Appl. Phys. Lett.* 91, 041907

15. Hicks EM, Lyandres O, Hall WP, Zou S, Glucksberg MR, VanDuyne RP **2007** Plasmonic Properties of Anchored Nanoparticles Fabricated by Reactive Ion Etching and Nanosphere Lithography *J. Phys. Chem. C* 111, 11, 4116-4124

16. Liu W, Zhong W, Qiu LJ, Lü LY, Du YW **2006** Fabrication and Magnetic Behaviour of 2D Ordered Fe/SiO_2 Nanodots Array *Eur. Phys. J. B* 51, 501-506

17. Djaoued Y, Badilescu S, Balaji S, Seirafianpour N, Hajiaboli A-R, Sadeghian RB, Braedley K, Brüning R, Kahrizi M, Truong V-V **2007** Micro-Raman Spectroscopy Study of Colloidal Crystal Films of Polystyrene-Gold Composites *Appl. Spectrosc.* 61, 1202-1210

18. Grassie N, Weir NA **1965** The Photooxidation of Polymers. III. Photooxidation of Polystyrene *J. Appl. Polymer Sci.* 9, 987-998

19. Grassie N, Weir NA **1965** The Photooxidation of Polymers. II. Photolysis of Polystyrene *J. Appl. Polymer Sci.* 9, 975-986

20. Guyot A **1986** Recent Developments in the Thermal Degradation of Polystyrene - A Review *Polym. Degr. Stab.* 15, 219-235

21. Workman Jr. J **2001** *Handbook of Organic Compounds: Vol. 2, UV-Vis and NIR Spectra* p. 223 Academic Press, San Diego

22. Venkatachalam RS, Boerio FJ, Carnevale MR, Roth PG **1988** Degradation of Polystyrene on Silver Substrates During Surface-Enhanced Raman Scattering *Appl. Spectrosc.* 42, 7, 1207-1213

23. Parry DB, Dendramis AL **1986** A High-Vacuum-Cell Approach to SERS Studies of Thin Films on Nonmetallic Surfaces *Appl. Spectrosc.* 40, 5, 656-661

24. Tuinstra F, Koenig JL **1970** Raman Spectrum of Graphite *J. Chem. Phys.* 53, 3, 1126-1130

25. Jasse B, Monnerie L **1975** Far-Infrared and Raman Spectra of Polystyrene Model Molecules *J. Phys. D Appl. Phys.* 8, 863-871

26. Jasse B, Chao RS, Koenig JL **1978** Laser Raman Scattering in Uniaxially Oriented Atactic Polystyrene *J. Polym. Sci. Polym. Phys. Ed.* 16, 2157-2169

27. Sears WM, Hunt JL, Stevens JR **1981** Raman Scattering from Polymerizing Styrene. I. Vibrational Mode Analysis *J. Chem. Phys.* 75, 4, 1589-1598

28. Nyquist RA, Putzig CL, Leugers MA, McLachlan RD, Thill B **1992** Comparison of the Vibrational Spectra and Assignments for α-Syndiotactic, β-Syndiotactic, Isotactic, and Atactic Polystyrene and Toluene *Appl. Spectrosc.* 46, 6, 981-987

29. Kellar EJC, Galiotis C, Andrews EH **1996** Raman Vibrational Studies of Syndiotactic Polystyrene. 1. Assignments in a Conformational/Crystallinity Sensitive Spectral Region *Macromolecules* 29, 3515-3520

30. Wilson Jr. EB **1934** The Normal Modes and Frequencies of Vibration of the Regular Plane Hexagon Model of the Benzene Molecule *Phys. Rev.* 45, 706-714

31. Felten A, Bittencourt C, Pireaux JJ, VanLier G, Charlier JC **2005** Radio-Frequency Plasma Functionalization of Carbon Nanotubes Surface O_2, NH_3, and CF_4 Treatments *J. Appl. Phys.* 98, 074308

32. Gaussian 03, Version 6.0; Frisch MJ, Trucks GW, Schlegel HB, Scuseria GE, Robb MA, Cheeseman JR, Montgomery Jr. JA, Vreven T, Kudin KN, Burant JC, Millam JM, Iyengar SS, Tomasi J, Barone V, Mennucci B, Cossi M, Scalmani G, Rega N, Petersson GA, Nakatsuji H, Hada M, Ehara M, Toyota K, Fukuda R, Hasegawa J, Ishida M, Nakajima T, Honda Y, Kitao O, Nakai H, Klene M, Li X, Knox JE, Hratchian HP, Cross JB, Bakken V, Adamo C, Jaramillo J, Gomperts R, Stratmann RE, Yazyev O, Austin AJ, Cammi R, Pomelli C, Ochterski JW, Ayala

PY, Morokuma K, Voth GA, Salvador P, Dannenberg JJ, Zakrzewski VG, Dapprich S, Daniels AD, Strain MC, Farkas O, Malick DK, Rabuck AD, Raghavachari K, Foresman JB, Ortiz JV, Cui Q, Baboul AG, Clifford S, Cioslowski J, Stefanov BB, Liu G, Liashenko A, Piskorz P, Komaromi I, Martin RL, Fox DJ, Keith T, Al-Laham MA, Peng CY, Nanayakkara A, Challacombe M, Gill PMW, Johnson B, Chen W, Wong MW, Gonzalez C, and Pople JA; Gaussian Inc, Wallingford CT; **2004**

33. Aroca R **2006** *Surface-Enhanced Vibrational Spectroscopy* p. 24 John Wiley & Sons, Chichester
34. Clark RJH, Hester RE **1988** *Advances in Spectroscopy: Vol. 16, Spectroscopy of Surfaces* p. 37-89 John Wiley & Sons, Chichester
35. Haruta M **2003** When Gold is Not Noble: Catalysis by Nanoparticles *Chem. Record* 3, 75-87
36. Della Pina C, Falletta E, Prati L, Rossi M **2008** Selective Oxidation Using Gold *Chem. Soc. Rev.* 37, 2077-2095
37. Valden M, Lai X, Goodman DW **1998** Onset of Catalytic Activity of Gold Clusters on Titania with the Appearance of Nonmetallic Properties *Science* 281, 1647-1650
38. Sanchez A, Abbet S, Heiz U, Schneider W-D, Häkkinen H, Barnett RN, Landman U **1999** When Gold is Not Noble: Nanoscale Gold Catalysts *J. Phys. Chem. A* 103, 9573-9578
39. Miller JT, Kropf AJ, Zha Y, Regalbuto JR, Delannoy L, Louis C, Bus E, van Bokhoven JA **2006** The Effect of Gold Particle Size on Au-Au Bond Length and Reactivity Toward Oxygen in Supported Catalysts *J. Catal.* 240, 222-234
40. Even if some of the gold clusters in our samples were smaller than 5 nm, and catalytically active, they would be too small to yield strong SERS (i.e., the size range for catalytic activity and the size range for SERS activity do not overlap). Therefore it would still be safe to say that the bands at 1183 and 1249 cm^{-1} in our spectra are not due to catalysis products.

Chapter 3: Scratched Gold Films

Reproduced in part with permission from *Plasmonics*: 2007, 2, 157-162.

3.1 Introduction

Increasing the order of the SERS substrate, we now move from gold clusters to scratched gold films. A unidirectional scratch, generated using a sharp tip, will consist of parallel nanostructures that resemble nanowires - each wire having a distinct diameter and shape.

It has already been demonstrated that for molecules adsorbed onto a scratched gold surface, SERS intensity is dependent upon the direction of incident-beam linear polarization relative to the scratches.[1,2] This anisotropy is not unique to scratched gold surfaces, but may be found wherever a SERS substrate has linear features. In addition to scratched gold films, polarization effects have been reported for silver nanowires,[3-5] silver nanorods,[6,7] and silver nanoparticle dimers.[8]

In reference 1, SERS intensity was found to vary with the polarization of the incident beam, relative to the direction of the scratch, in a $\sin^2$ or $\cos^2$ way: SERS intensity was greatest when light was polarized across the scratch and minimal when light was polarized along the scratch.

The qualitative aspect of this result may be understood by recalling that a rough, nanostructured surface is necessary for SERS; and noting that light interacts with a rough surface in the perpendicular orientation but not in the parallel orientation.

The quantitative aspect of this result may be understood by referring to section 1.2.3. There it was said that SERS intensity scales with a squared term for the enhancement of incident light (Equation 1.2), and another squared term for the enhancement of scattered light (Equation 1.4). Consequently, $\sin^2$ and $\cos^2$ fits were compared to $\sin^4$ and $\cos^4$ fits in reference 1. The better fits acquired using $\sin^2$ and $\cos^2$ suggest that the outgoing light has no preferred polarization, and thus enhancement of the outgoing light does not depend on the direction of incident-beam polarization.

In this chapter we examine the polarization-dependent enhancement effect associated with scratched gold films placed in an electrochemical cell (placed *in-situ* and under potential control). A quantitative method for evaluating the extent of a polarization effect will be proposed. In addition, it will be shown that the polarization effect can be used to eliminate a solution-phase interference signal without removing the signal from an adsorbed analyte.

Proof of concept was carried out using oxazine 720 and perchlorate. The laser dye oxazine 720 was chosen to represent an adsorbed analyte because it has a very high cross-section. This is due, in part, to an electronic absorption band that lies in resonance with our He-Ne excitation source. Perchlorate was used to represent a solution-phase interference because it does not adsorb onto gold.

Following proof of concept, the principles developed in this chapter will be used to monitor the electrochemically-driven desorption and readsorption of cysteine.

Cysteine was chosen for a variety of reasons. As an amino acid, it is a simple molecule of biological interest. It has a $-CH_2SH$ R-group, and may therefore bond to gold through its sulfur atom. It does not have an absorption band that lies in resonance with our He-Ne excitation source, an advantage because fluorescence from a resonant species can mask the ordinary Raman signal from molecules in solution.

Finally, we note that scratched gold films are cheap and easy to produce. They are worthy of study because they may be appropriate for sensors that require a disposable SERS substrate.

3.2 Experimental Methods

Glass slides plated with 5 nm of chromium and 100 nm of gold were obtained from Evaporated Metal Films (EMF). These slides were scratched by manually running a 10 µm metallic tip along the surface of the gold. An atomic force microscope (AFM) image of a scratch produced in this way is presented in Figure 3.1.[1] The image shows that a set of parallel gold nanowires, with a random distribution of sizes and shapes, are formed within the scratch.

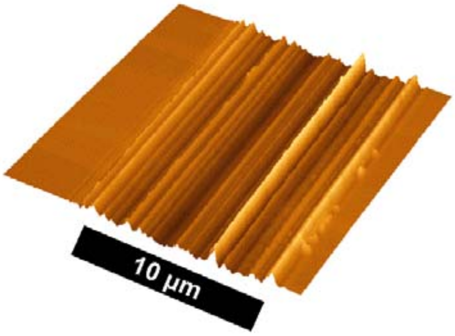

Figure 3.1 An AFM image of a scratch in a gold film.

Oxazine 720 (from Lambdachrome) was dissolved in ethanol to create a 10 µM solution. A slide was held at an angle while a single drop of the oxazine 720 solution was added to its gold surface and allowed to run overtop of the scratched area. After the solvent evaporated, the slide was rinsed with ultrapure water (18.2 MΩ cm, from a Barnstead NANOpure Diamond water purification system).

Preliminary experiments to confirm the polarized nature of the scratches were carried out using the experimental setup shown in Figure 3.2a. The rest of the work presented in this chapter was conducted using the setup shown in Figure 3.3. The equipment depicted in Figure 3.3, and the associated procedures employed, will now be described.

The gold slide, modified with oxazine 720, was placed in a custom-made Teflon electrochemical cell prepared in house. The cell was filled with a 0.1 M $NaClO_4$ / 0.1 M NaCl aqueous electrolyte solution, and placed under an Olympus BHT optical microscope set up to collect Raman spectra in a backscattering geometry.

A 35 mW He-Ne laser from Melles Griot provided 632.8 nm light. The beam passed through a ½-wave plate, entered the microscope through an optical inlet, was reflected by the scratched gold surface, and exited the microscope through an optical outlet. An Olympus MS Plan 50 × ultra-long working distance (ULWD) microscope objective with numerical aperture 0.55 was used to focus the laser onto the sample. This same lens was used to collect scattered and reflected light. A Kaiser super-notch filter was used to exclude most of the Rayleigh light. The remaining light, which contained Raman information, was directed by a Kaiser Holospec $f/1.4$ spectrograph onto an Andor DV-401-BV CCD. The diameter of the laser spot was approximately equal to the scratch width, about 10 μm.

A broad fluorescence background signal was obtained for slides modified with oxazine 720. It is well known that fluorescence from molecules in contact with a metal surface is efficiently quenched,[9,10] so the fluorescence background implies that a multilayer of oxazine 720, rather than a monolayer, was deposited by using the procedure described above. To minimize this signal, the area to be investigated was irradiated with

He-Ne laser light for 1 hour before accumulation of SERS data began. Due to photobleaching of the dye, a steady decline in fluorescence intensity was observed during this time. The fluorescence background was substantially decreased and time-stable after this treatment.

For the blank experiments, scratched gold surfaces without oxazine 720 adsorbed were immersed in a 0.2 M $NaClO_4$ aqueous electrolyte solution.

A potential difference was established between the scratched gold film and the electrolyte solution using a Hokuto Denko Limited potentiostat/galvanostat, model HAB-151, so that the polarization effect could be examined over a range of applied potentials.

During the proof of concept experiments involving oxazine 720 and perchlorate (section 3.3.1), the gold surface of the slide acted as the working electrode and a circular platinum wire acted as the counter electrode. A silver wire coated with silver chloride acted as the reference electrode.

In section 3.3.2, the principles developed in section 3.3.1 are applied to an electrochemically-driven desorption/readsorption process. The following system was used: 0.9 M DL-cysteine in an aqueous solution 0.2 M in $NaClO_4$ and 0.5 M in NaOH (the pH of this solution was measured to be 8.47). The working electrode was a scratched gold film and the counter electrode was a circular platinum wire. The reference electrode was a platinum wire; however, potentials were corrected to simulate a pseudo silver / silver chloride reference so as to be consistent with the other results presented in this chapter. The DL-cysteine was obtained 97 % pure from Aldrich.

3.3 Results and Discussion

3.3.1 Proof of Concept Using Oxazine 720 and Perchlorate

Preliminary experiments to confirm the polarized nature of the scratches were conducted before the *in-situ* spectroelectrochemical ones. These preliminary experiments are summarized in Figure 3.2. Two sets of scratches, with direction perpendicular to each other, were produced in a gold film and coated with the Raman-active dye molecule oxazine 720. A pair of microscope objectives focused He-Ne laser light onto the scratched gold surfaces, through air, in a forward scattering geometry (Figure 3.2a). A ½-wave plate was used to rotate the plane of incident-beam polarization through angles which are defined in Figure 3.2b. In Figure 3.2c, a polar plot shows the dependence of SERS intensity on the relative orientation between incident-beam polarization and scratch direction for the 596 cm^{-1} band of oxazine 720. SERS intensity (in arbitrary units) is plotted along the radius of the circle, and relative orientation (in degrees) is plotted along the circumference. The solid curves represent $\cos^2$ and $\sin^2$ fits to the experimental data points: diamonds and squares respectively. The data shown graphically in Figure 3.2c is given in Appendix A. Maximum SERS intensity was obtained at approximately 0° and 180° for scratch orientation a (diamonds), and at approximately 90° and 270° for scratch orientation b (squares).

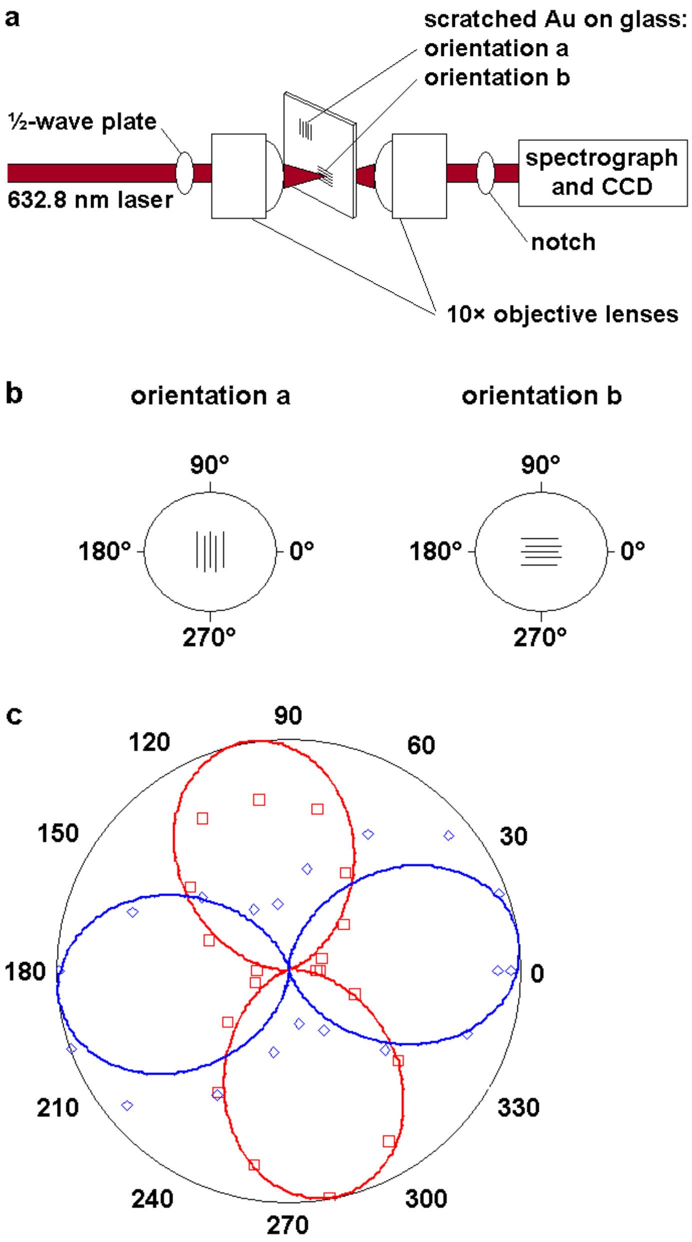

Figure 3.2 (a) The apparatus used to carry out preliminary experiments on scratched gold films. (b) The angle of rotation for incident-beam polarization is defined with respect to scratch orientations a and b. (c) Polar plots show the dependence of SERS intensity on incident-beam polarization for scratch orientation a (diamonds) and orientation b (squares).

A photon in free space and a photon bound to the surface of a noble metal (a surface plasmon or SP) do not normally interconvert because the former does not possess as much momentum as the latter.[11] If a grating is present in the surface of the metal, this momentum mismatch can be overcome.[11]

The preliminary results in Figure 3.2c indicate that the parallel nanostructures within a scratch can act as a crude grating. In other words, the random parallel nanowires can be thought of as a Fourier superposition of a number of oriented gratings of different periodicity that maintains the polarization properties of the original set. When the polarization of incident light is perpendicular to the long axis of the scratches, SPs may travel across the corrugations and enhanced EM field will occur in areas of high curvature and in the space between metal nanostructures. Raman-active molecules adsorbed in these areas will give a strong SERS signal, as shown in Figure 3.2c.

When the polarization of incident light is parallel to the long axis of the scratches, SPs are not expected and SERS should not be observable because the crude grating is absent. Parallel-alignment SERS peaks were found to be less intense than the corresponding perpendicular-alignment ones, however, signal intensity obtained for the parallel alignment was non-zero (diamond and square data points in Figure 3.2c do not pass through the centre of the polar plots). A small amount of field enhancement does occur in the parallel orientation because some of the nanometer-sized features within the scratched area are randomly oriented. These can be regarded as defects which arise from the simple procedure employed for scratch generation. Also, alignment between the scratches and the incident beam is subject to some error and this explains the tilt-angle of about 10° in the polar plots.

An electronic absorption band of oxazine 720 is centered at 620 nm, and this transition is in resonance with the 633 nm excitation wavelength employed.[12] I.e., it is actually surface-enhanced resonance Raman scattering (SERRS) that we observe from oxazine 720 on scratched gold when a Ne-Ne laser is used as the excitation source. No signal was obtained from oxazine 720 adsorbed on smooth gold; and since resonance Raman scattering from molecules on the smooth surface is expected, the absence of signal implies that a very small amount of dye was left on the metal by the application procedure reported here.

In order to explore the polarization effect described above for background suppression, the scratched gold film was incorporated into a custom made Teflon cell and the cell was placed under an optical microscope (Figure 3.3). The cell was then filled with an aqueous solution of sodium perchlorate electrolyte. Oxazine 720 was used as the adsorbed Raman-active molecule and it represents some potential analyte in an electrochemical SERS experiment. The perchlorate anion is also Raman-active, but it is not adsorbed onto the gold surface and it represents a solution-phase interference.

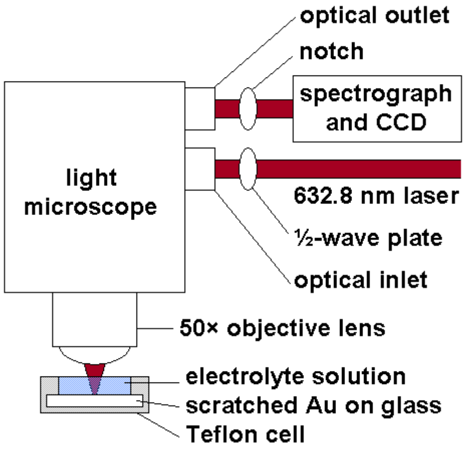

Figure 3.3 The experimental setup used to examine polarization-dependent SERS from scratched gold films.

The premise of the proposed methodology for background subtraction is that the polarization-dependent enhancement will be observed for Raman-active molecules adsorbed onto the surface but not for those in the solution phase. This is because SPs, which cause the enhancement, are basically surface-confined. Since the perchlorate anion is not adsorbed, it does not give rise to a polarization-dependent SERS signal and only an ordinary Raman signal is observed. A caveat for this is the fact that the SP field decays exponentially with distance from the surface.[11] When the polarization of the light is perpendicular to the scratched metal surface (and SERS is operative) some of the solution species will be within the SP field. The main contribution to the overall signal will come from the adsorbed species, however, because the SP field is maximum at the surface and decays fast within a few nanometers. The SERS is not as significant when polarization of the laser is parallel to the scratches. In this case, the contribution from the adsorbed species is drastically reduced, but the ordinary Raman signal from the solution species is not significantly changed.

Figure 3.4 shows the Raman spectra of perchlorate in solution above a scratched gold surface that was not treated with oxazine 720. The electrochemical potential was held at 0 mV. The 934 cm^{-1} band is due to the completely symmetric stretch of the ion. The spectra $S_{\perp}$ and $S_{//}$ were obtained with the incident beam polarized across and along the scratches, respectively.

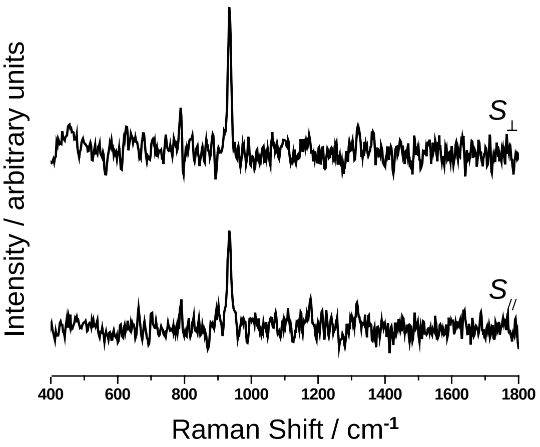

Figure 3.4 $S_\perp$ and $S_{//}$ for perchlorate, which represents an interference in the solution above the analyte. Acquisition time was 45 s. These spectra were baseline-corrected; the uncorrected spectra appear in Appendix A.

It can be seen, by comparing spectra $S_\perp$ and $S_{//}$ in Figure 3.4, that perchlorate band intensity changes with the direction of incident-beam polarization relative to the direction of the scratch. There are two possible reasons for this change. It may be that some perchlorate anions, though in solution, still lie within the decaying field of the SPs and are therefore subject to a small polarization effect. The other possibility is that some optical anisotropy is introduced by the microscope.

To determine if the microscope introduces an artificial polarization effect, the laser spot was focused on a smooth gold surface. A “real” polarization effect is impossible here because the scratches that give rise to polarization-dependent SERS are absent. When the ½-wave plate was rotated to positions used for perpendicular- and parallel-geometry data acquisition, a difference in intensity between the spectra $S_\perp$ and $S_{//}$ was indeed observed. This means that optical components within the microscope result in a polarization bias, likely because s- and p-polarizations are reflected from them with different efficiencies.[13]

Figure 3.5 shows the Raman spectrum for oxazine 720 drop-coated onto a scratched gold slide, then placed *in-situ* and under electrochemical control (0 mV). The difference between $S_\perp$ and $S_{//}$ was much greater for oxazine 720 (Figure 3.5) than it was for perchlorate anion (Figure 3.4) and this indicates that oxazine 720 molecules are located in areas where the polarization-dependent surface-enhancement effect is operative (i.e., SERS was observed for oxazine 720 whereas an ordinary Raman spectrum was observed for perchlorate).

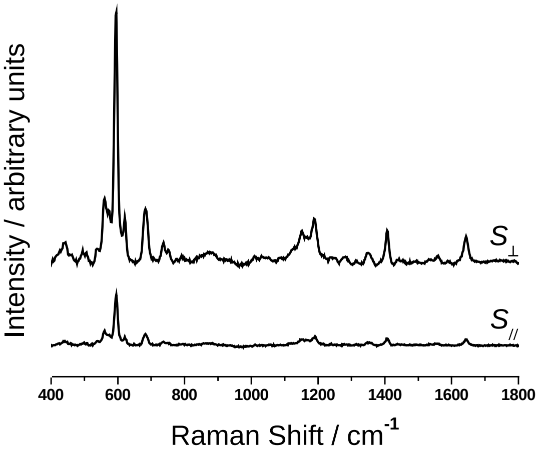

Figure 3.5 $S_\perp$ and $S_{//}$ for oxazine 720, which represents an analyte on the surface of the metal. Acquisition time was 20 s. These spectra were baseline-corrected; the uncorrected spectra appear in Appendix A.

Perchlorate was present in the aqueous solution above the slide, but its signal is masked by the far greater one from oxazine 720. The experimental set-up was the same for oxazine 720 as it was for perchlorate, so the anisotropy introduced by the microscope is expected to affect $S_{\perp}$ and $S_{//}$ in Figure 3.5 to the same extent as it did $S_{\perp}$ and $S_{//}$ in Figure 3.4.

Equation 3.1 is now proposed in an attempt to quantify the extent of an observed polarization effect.

$$p_{observed} = \frac{I_{\perp} - I_{//}}{I_{\perp} + I_{//}} \qquad (3.1)$$

Here $I_{\perp}$ is the intensity of a Raman band obtained using a perpendicular alignment of incident-beam polarization with scratch direction, and $I_{//}$ is the intensity of the same band obtained using a parallel alignment. This approach allows an empirical polarization effect to be quantified on a scale ranging from 0 to 1. The best possible polarization effect would yield a large value for $I_{\perp}$ and a null value for $I_{//}$, therefore the ideal value for $p_{observed}$ is 1. No polarization effect would yield $I_{\perp} = I_{//}$, and a $p_{observed}$ value of 0.

However, a correction factor f is required to compensate for artificial polarization effects from the microscope.

$$f = \frac{I'_{\perp}}{I'_{//}} \qquad (3.2)$$

In Equation 3.2, a prime indicates the intensity must be measured under conditions where a "real" polarization effect is impossible (a smooth area on the surface of the metal must be used).

Equation 3.1 thus becomes Equation 3.3, and $p_{observed}$ ranges from 0 to 1 in the microscope experiment.

$$p_{observed} = \frac{I_{\perp} - f \cdot I_{//}}{I_{\perp} + f \cdot I_{//}} \tag{3.3}$$

As stated earlier, the polarization-dependent enhancement effect can be used to eliminate the Raman band of a solution-phase interference (represented here by perchlorate) without removing the SERS band of some adsorbed analyte (represented by oxazine 720). The background subtraction is accomplished by obtaining a mathematically manipulated spectrum for analytical purposes, $S_{analytical}$, using Equation 3.4.

$$S_{analytical} = S_{\perp} - f \cdot S_{//} \tag{3.4}$$

Here $S_{\perp}$ is the entire spectrum obtained using a perpendicular alignment, $S_{//}$ is the entire spectrum obtained using a parallel alignment, and *f* from Equation 3.2 is a constant applied to each data point in $S_{//}$. In this study, *f*-values obtained for perchlorate in solution over a smooth gold surface were used to correct $S_{//}$ for both oxazine 720 and perchlorate.

When Equation 3.4 was applied to the ordinary Raman signal obtained from perchlorate dissolved in the solution above the scratched gold surface (Figure 3.4), the perchlorate peak was eliminated (Figure 3.6a). When it was applied to the SERS signal obtained from oxazine 720 adsorbed onto the scratched gold surface (Figure 3.5), oxazine 720 peaks persisted (Figure 3.6b).

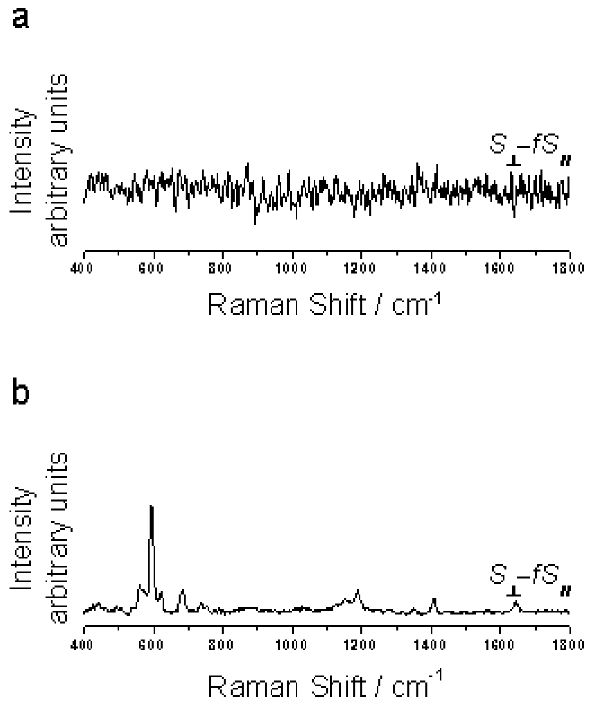

Figure 3.6 (a) $S_{analytical}$ was obtained for perchlorate using the $S_\perp$ and $S_{//}$ spectra shown in Figure 3.4. The interference signal is eliminated by use of Equation 3.4. (b) $S_{analytical}$ was obtained for oxazine 720 using the $S_\perp$ and $S_{//}$ spectra shown in Figure 3.5. The analyte signal is retained.

Although areas of the metal treated with oxazine 720 were irradiated with the He-Ne laser for 1 hour before any spectra were accumulated from them, some oxazine 720 fluorescence remained (see section 3.2). It should be noted that this fluorescence persists in $S_{analytical}$ if $S_\perp$ and $S_{//}$ are not baseline-corrected. Uncorrected $S_\perp$ and $S_{//}$, as well as the resulting $S_{analytical}$, are shown for oxazine 720 and perchlorate in Appendix A.

The 596 cm^{-1} peak was used to calculate $p_{observed}$ values for oxazine 720, and the 934 cm^{-1} peak was used for perchlorate. In each case, $p_{observed}$ values were fairly constant and reproducible over the potential range investigated: +300 to –300 mV for oxazine 720 and +300 to –900 mV for perchlorate. This is shown in Figure 3.7 (each point is an average of two, and error bars mark the standard deviation obtained from all $p_{observed}$ values for oxazine 720 or all $p_{observed}$ values for perchlorate). Potentials below –300 mV were not examined for oxazine 720 because desorption, evidenced by an increase in fluorescence, was found to occur there.[12] The $p_{observed}$ values of about 0.4 for oxazine 720 and 0.0 for perchlorate indicate that a polarization effect exists for the former and not the latter.

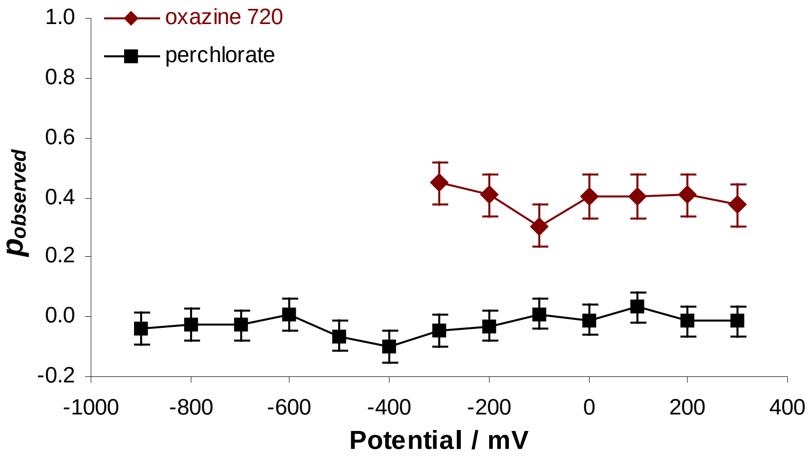

Figure 3.7 Values of $p_{observed}$ for oxazine 720 and perchlorate remain fairly constant and reproducible with changes in potential.

Figure 3.7 indicates that our procedure (Equation 3.4) is applicable to electrochemical studies provided the interfering species (perchlorate in our case) is not adsorbed or electrochemically active within the potential range investigated. The study of water structure in the double layer region by SERS[14] is a good candidate for our methodology, since the SERS signal from water is inherently weak and can sometimes be overwhelmed by the ordinary Raman signal from the solvent.

3.3.2 Application to the Electrochemically-Driven Desorption and Readsorption of Cysteine

Thus far we have presented only a proof of concept - clearly there is no overlap between the 934 cm^{-1} perchlorate band and any of the higher intensity oxazine 720 bands.

We now move to a system in which a single compound (cysteine) plays both the role of the adsorbate and that of the solution-phase species.

A potential dependent polarization effect was found to occur for cysteine dissolved in a basic, aqueous solution of sodium perchlorate. Figure 3.8 shows the potential dependence of $p_{observed}$ for cysteine's 688 cm^{-1} band, which is due to the C-S stretch. Figure 3.9 shows $S_{\perp}$, $S_{//}$ and $S_{analytical}$ for this band where $p_{observed}$ is maximum (-392 mV in the negative sweep) and minimum (-692 mV in the positive sweep). The raw data used to create Figure 3.9 appears in Appendix A.

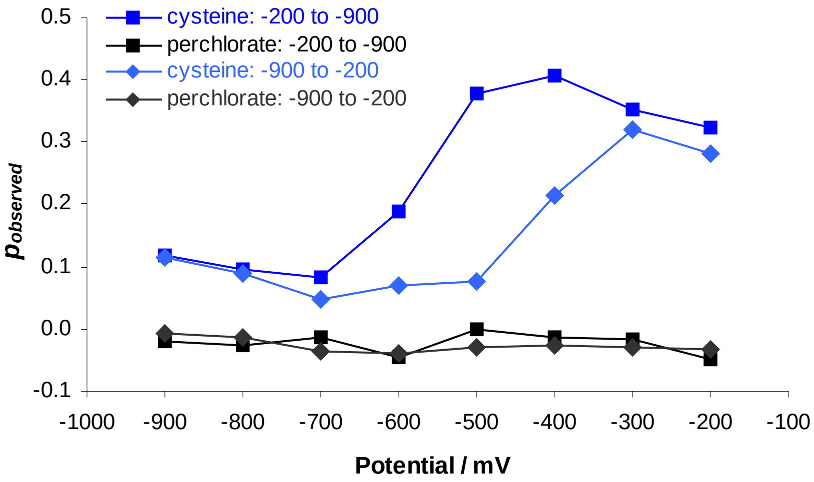

Figure 3.8 Values of $p_{observed}$ for cysteine's 688 cm^{-1} band are potential dependent.

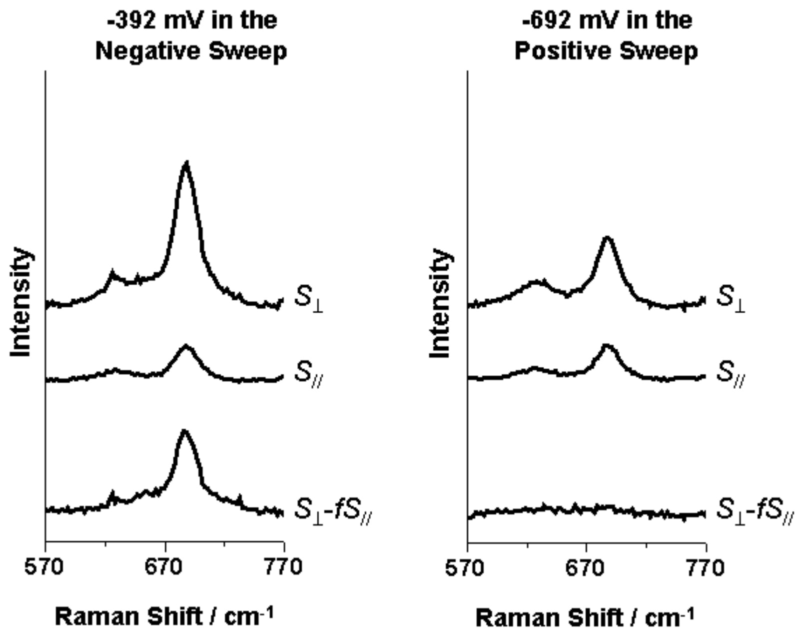

Figure 3.9 $S_\perp$, $S_{//}$ and $S_{analytical}$ for cysteine. Acquisition time was 180 s. $S_\perp$ and $S_{//}$ were baseline-corrected; the uncorrected spectra appear in Appendix A.

One possible explanation for this experimental result is a desorption/readsorption process, with desorption (evidenced by a decrease in $p_{observed}$) occurring in the negative sweep and readsorption (evidenced by an increase in $p_{observed}$) occurring in the positive sweep. Reasons for this proposed explanation are given below.

First, the potential range in Figure 3.8 is about right for a desorption/readsorption process. The desorption/readsorption of cysteine from gold reportedly occurs between -600 to -700 mV relative to a saturated calomel electrode (SCE).[15] The potential range in Figure 3.8, -300 to -700 mV relative to a pseudo silver / silver chloride reference electrode, corresponds to a range of -325 to -725 mV relative to an SCE.

Second, $S_{analytical}$ for the maximum and minimum $p_{observed}$ data points are consistent with the idea of a desorption/readsorption process. $S_{analytical}$ from the -392 mV negative-sweep data point shows that some bands are more sensitive to polarization than others

(Appendix A). Vibrational modes associated with functional groups lying closer to the surface of the metal will display a stronger polarization effect, so this result suggests that cysteine is adsorbed and has a preferred orientation with respect to the surface. $S_{analytical}$ from the -692 mV positive-sweep data point shows that all bands are equally insensitive to the polarization effect (Appendix A). This suggests that cysteine is desorbed and has a random orientation with respect to the surface while in solution. The reason why $p_{observed}$ is $\neq 0$ for potentials $\leq$ -700 mV is probably because our solution is so concentrated that a significant amount of solution-phase cysteine remains in the SP field after desorption.

3.4 Conclusions

Scratched gold films display polarization-dependent SERS. In this chapter, a method for quantifying the polarization-dependence was introduced. Polarization artifacts can arise from the light microscope employed in Raman microscopy; however, it is easy to remove these artifacts mathematically by using a reference signal from a smooth surface. It was successfully demonstrated that scratched gold slides and a polarized excitation source may be used to eliminate solution-phase interference signals from the spectrum of an adsorbed analyte, and it was shown that the methodology is applicable to electrochemical SERS studies. Following proof of concept with oxazine 720 and perchlorate, our method was applied to the electrochemically-driven desorption and readsorption of cysteine.

The use of polarization-dependent SERS for removal of solution-phase interference signals is preferable to the more customary subtraction of a solution spectrum (obtained using a smooth surface) from one containing both SERS and solution-phase information (obtained using a rough surface). This is because rotation of a ½-wave plate is less awkward, and subject to less error, than locating and relocating a particular μm-scale area on an inhomogeneous SERS substrate. Automation, and therefore real-time measurement, is more easily accomplished using our method because signal and background are accumulated from the same location.

Finally, the gold plated glass slides used here are cheap, and the scratches are easy to fabricate. Therefore, scratched metallic films of this type might be appropriate for analytical devices that require a disposable SERS substrate.

3.5 References and Notes

1. Brolo AG, Arctander E, Addison CJ **2005** Strong Polarized Enhanced Raman Scattering Via Optical Tunneling Through Random Parallel Nanostructures in Au Thin Films *J. Phys. Chem. B* 109, 401-405
2. Brolo AG, Addison CJ **2005** Surface-Enhanced Raman Scattering from Oxazine 720 Adsorbed on Scratched Gold Films *J. Raman Spectrosc.* 36, 629-634
3. Jeong DH, Zhang YX, Moskovits M **2004** Polarized Surface Enhanced Raman Scattering from Aligned Silver Nanowire Rafts *J. Phys. Chem. B* 108, 12724-12728
4. Moskovits M, Jeong DH **2004** Engineering Nanostructures for Giant Optical Fields *Chem. Phys. Lett.* 397, 91-95
5. Tao AR, Yang P **2005** Polarized Surface-Enhanced Raman Spectroscopy on Coupled Metallic Nanowires *J. Phys. Chem. B* 109, 15687-15690
6. Martínez JL, Gao Y, López-Ríos T **1987** Anisotropic Surface-Enhanced Raman Scattering at Obliquely Evaporated Ag Films *Phys. Rev. B* 35, 18, 9481-9488
7. Zhao Y-P, Chaney SB, Shanmukh S, Dluhy RA **2006** Polarized Surface Enhanced Raman and Absorbance Spectra of Aligned Silver Nanorod Arrays *J. Phys. Chem. B* 110, 3153-3157
8. Xu H, Käll M **2003** Polarization-Dependent Surface-Enhanced Raman Spectroscopy of Isolated Silver Nanoaggregates *ChemPhysChem* 4, 1001-1005

9. Gersten J, Nitzan A **1981** Spectroscopic Properties of Molecules Interacting with Small Dielectric Particles *J. Chem. Phys.* 75, 3, 1139-1152
10. Dulkeith E, Morteani AC, Niedereichholz T, Klar TA, Feldmann J, Levi SA, van Veggel FCJM, Reinhoudt DN, Möller M, Gittins DI **2002** Fluorescence Quenching of Dye Molecules Near Gold Nanoparticles: Radiative and Nonradiative Effects *Phys. Rev. Lett.* 89, 203002
11. Barnes WL, Dereux A, Ebbesen TW **2003** Surface Plasmon Subwavelength Optics *Nature* 424, 824-830
12. Brolo AG, Sanderson AC **2004** Surface-Enhanced Raman Scattering (SERS) from a Silver Electrode Modified with Oxazine 720 *Can. J. Chem.* 82, 1474-1480
13. Kingslake R, ed. **1965** *Applied Optics and Optical Engineering: Vol. 1, Light: Its Generation and Modification* Academic Press Inc, New York
14. Wu D-Y, Li J-F, Ren B, Tian Z-Q **2008** Electrochemical Surface-Enhanced Raman Spectroscopy of Nanostructures *Chem. Soc. Rev.* 37, 1025-1041
15. Hager G, Brolo AG **2009** Protonation and Deprotonation of Cysteine and Cystine Monolayers Probed by Impedance Spectroscopy *J. Electroanal. Chem.* 625, 109-116

Chapter 4: Nanohole Arrays in a Copper Film

Reproduced in part with permission from *J. Phys. Chem. C*: 2008, 112, 17051-17055.

4.1 Introduction

Increasing the order of the SERS substrate still further, we move from scratches (which possess some order) to nanohole arrays (which are periodic in two dimensions, and fabricated with a high degree of precision). As stated in section 1.3.2, nanohole arrays are of special interest because they are closely associated with a phenomenon called extraordinary optical transmission (EOT).

EOT was first reported in 1998 by Ebbesen et al.[1] In EOT, the absolute transmission efficiency for light passing through subwavelength hole arrays in optically thick metal films was reported to be ≥ 2 at the transmission peak maxima. A connection between EOT and surface plasmons (SPs) was immediately recognized.[1]

SPs are fluctuations in electron density that propagate along the surface of a noble metal and yield localized regions of high electromagnetic fieldstrength (section 1.2.3). A photon bound to the surface of a metal (i.e., a SP) has more momentum than a photon in free space; hence, the two cannot interconvert unless a momentum-matching process is operational. When a periodic nanohole array is present, the momentum matching condition is satisfied for each diffraction order and this has been termed grating coupling.[2-5]

A simplified view of the EOT mechanism is as follows: incident photons are converted to SPs on one side of the metal film at wavelengths where the Bragg condition is satisfied; propagating SPs scatter at the hole edges, transferring energy through the holes; SPs are then converted back to photons on the other side of the film.[6] A comprehensive theory of EOT that takes into account the relative role of SP modes and other electromagnetic fields involved in the phenomenon has recently been published.[7]

Since the discovery of EOT, optical and spectroscopic effects associated with these subwavelength structures have become the subject of intense investigation.[2-4,8] In addition to the push for a better understanding of the phenomenon itself, some very attractive applications have been realized in the areas of nanolithography,[9] optoelectronics,[10] and chemical sensing.[11-15]

It is generally accepted that SPs are primarily responsible for SERS, due to the extreme electromagnetic field localization that accompanies SP excitation (section 1.2.2 and section 1.2.3). Since SPs are responsible for both EOT through nanohole arrays and SERS, a Raman-active compound present on the surface of a nanohole array should be expected to show SERS. This is indeed the case, and was reported by our group in 2004.[16] Others have since confirmed that nanohole arrays may act as a substrate for SERS.[17-20]

A few studies of subwavelength hole arrays in copper have been conducted,[21-23] but they are far more rare than those which employ gold or silver. Gold and silver offer different advantages over copper. Gold is more stable chemically, whereas copper surfaces are generally covered with oxides and other contaminant layers. Silver allows more efficient SP propagation than does copper, as the imaginary part of the silver dielectric constant is significantly smaller than that of the copper dielectric constant ($\mathrm{Im}[\varepsilon_{Ag}] < \mathrm{Im}[\varepsilon_{Cu}]$) in the visible region of the spectrum.[24]

On the other hand, copper is the most abundant metal that can support SP excitation by visible light. It is therefore important to study the plasmonic properties of copper structures, as this metal may provide a cheaper alternative to silver and gold for certain applications.

In this chapter, we show that an array of subwavelength holes in copper can indeed be used as a substrate for SERS. The effect of inter-hole distance (hole-periodicity) on SERS intensity, in both forward and backscattering geometries, will be presented.

Calculations were performed using a simplified relationship[25] between SP resonance wavelength and hole-periodicity. In addition, the electric field intensity responsible for SERS was calculated for each periodicity using the finite-difference time-domain (FDTD) method. Both levels of theory accurately predict which periodicity will give the greatest SERS intensity, as observed by experiment.

4.2 Experimental Methods

4.2.1 Copper Deposition

A glass slide was sonicated for 10 minutes in methanol and 10 minutes in ultrapure water (18.2 MΩ cm resistivity from a Barnstead NANOpure Diamond water purification system). It was then submersed in piranha solution (3:1 concentrated sulfuric acid : 30 % aqueous hydrogen peroxide) for 30 minutes, rinsed with ultrapure water, and blown dry with a stream of 99.998 % pure nitrogen.

The glass slide was then placed in a chamber used for depositing metal by high-temperature evaporation. A 4.8 nm chromium adhesion layer was deposited onto the glass at a rate of about 2 or 3 nm/s, and a 144 nm copper film was deposited onto the chromium layer at a rate of about 3 or 4 nm/s. Metal thickness was measured using a quartz crystal microbalance (QCM). The copper used for vapour deposition was obtained 99.999 % pure from Aldrich.

The 4.8 nm chromium adhesion layer will suppress SP modes on the copper-chromium side of the sample,[26] as the imaginary part of the chromium dielectric constant is quite high in the vicinity of the excitation wavelength (633 nm).[27] We did not attempt to prepare a sample without the adhesion layer because nanohole-fabrication was carried out at another institution (Simon Fraser University in Burnaby), and we were concerned that damage to the sample might occur during transit if this layer was left absent.

4.2.2 Fabrication of the Nanohole Arrays and Confirmation of the Copper Film Thickness

Nanohole arrays were fabricated and imaged using an FEI 235 focused ion beam (FIB) - scanning electron microscope (SEM) dualbeam instrument. Eight square arrays were made with varying hole-periodicity: 362, 415, 475, 522, 578, 629, 681, and 737 nm. The average hole diameter was 133 nm.

A trench was milled in the copper film by FIB and imaged by SEM. Trench-depth measurements made from the SEM image confirmed the film thickness that was given by the QCM during vapour deposition.

4.2.3 Application of Oxazine 720

Oxazine 720 was chosen to be the probe in our SERS experiments. The ordinary Raman and the SERS of this compound, on gold and on silver, have been studied by our group.[16,28] Oxazine 720 was applied to the nanohole arrays in the following way: one edge of the copper-on-glass sample was lifted so that it lay at an angle; a drop of 90 μM oxazine 720 (from Lambdachrome) in methanol was applied to the sample above the nanohole arrays and allowed to run down over the surface of the copper where the arrays were milled; the copper surface was then rinsed with plenty of ultrapure water and blown dry with nitrogen.

4.2.4 SERS Setup

SERS experiments were conducted in both forward and backscattering geometries (Figure 4.1).

The backscattering geometry is shown in Figure 4.1a. Here, 632.8 nm light from a 35 mW Melles Griot He-Ne laser was directed into an Olympus BHT microscope and focused onto each nanohole array from the copper side of the sample using a 50 × objective lens (numerical aperture 0.80). Backscattered light was collected by this same objective lens, directed out of the microscope, through a Kaiser super-notch filter, through a Kaiser Holospec *f*/1.4 spectrograph, and onto an Andor DV-401-BV CCD detector. The laser spot was adjusted to fill an array without exceeding its edges; spot diameter was approximately 10 µm. Each array was positioned so that two edges lay parallel (and two edges lay perpendicular) to the polarization of the incident beam. Accumulation time was set at 20 s.

The forward-scattering geometry is shown in Figure 4.1b. Light from the He-Ne laser was focused onto each array from the glass side of the sample using a 10 × objective lens (numerical aperture 0.25). The 50 × objective lens was used on the copper side of the sample to collect the scattered light. Note that in the forward-scattering geometry, light needs to pass through the array to excite oxazine 720 molecules. After collection by the 50 × objective lens, transmitted light followed the same path to the CCD as did light in the backscattering-geometry experiment. The laser spot was approximately 10 µm in diameter, and two edges of an array were positioned parallel to the polarization of the incident beam during acquisition. Accumulation time was set at 120 s.

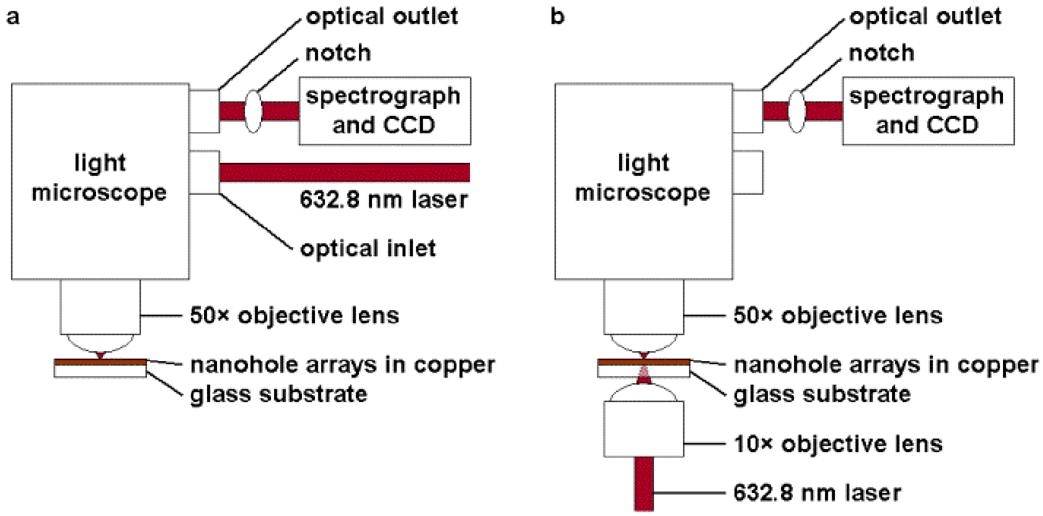

Figure 4.1 The experimental setup for acquisition of SERS data in (a) the backscattering geometry and (b) the forward-scattering geometry.

4.2.5 FDTD Calculations

FDTD is a numerical method for modeling the way electromagnetic fields interact with objects, based on their material properties, by solving Maxwell's equations. It is commonly used by electrical engineers, and we therefore collaborated with Pramodha Marthandam and Reuven Gordon (Department of Electrical Engineering at the University of Victoria), who ran the FDTD simulations and provided us with the output files.

Calculations were performed using Lumerical FDTD Solutions software hosted by the Westgrid high performance computer cluster. The simulations were set up with periodic boundary conditions along the x and y-directions, and perfectly matched layers along the z-direction, with the z-boundaries being placed 500 nm above and 400 nm below the metal surface. A grid size of $25 \times 25 \times 25\ nm^3$ was chosen for the overall simulation volume, with a small region 5 nm above the copper surface and 10 nm below the copper surface into the metal, extending over the entire x and y-span of the simulation boundary, having grid sizes of 10 nm along the x and y-directions and 5 nm along the z-direction. The grid size in the region close to the metal surface was chosen to best capture the SP fields. The larger mesh was chosen everywhere else to help minimize computation time. Polarization of the incident laser was set parallel to the x-axis, and simulations were carried out for both forward and backscattering geometries. Monitors were placed on both the copper-air and copper-chromium interface sides to measure the fields in both geometries. The simulation time was set at 150 fs, for an input pulse width of 20 fs. This was chosen to allow the fields to decay completely before termination of the simulations. The source was placed 25 nm from the z-boundary in each corresponding scattering geometry. A Drude-Lorentz model was used to capture the dispersion of copper,[24] however the chromium was assumed to be dispersionless.

4.3 Results and Discussion

Subwavelength hole arrays were milled in a copper film, and eight different hole periodicities were examined: 362, 415, 475, 522, 578, 629, 681, and 737 nm. SEM images of the 578 nm periodicity array are presented in Figure 4.2. Oxazine 720, a Raman-active dye molecule, was applied to the arrays for use as a probe. SERS spectra were then collected from each array in both the forward and backscattering geometries (Figure 4.1). The spectrum of oxazine 720 adsorbed on nanoholes in copper is shown in Figure 4.3.

Although the SERS obtained from these arrays was not strong, the 596 cm^{-1} band of oxazine 720 was clearly visible in each spectrum. No signal was detected from oxazine 720 on the unpatterned copper surface (in the backscattering geometry), thus confirming enhancement from the arrays.

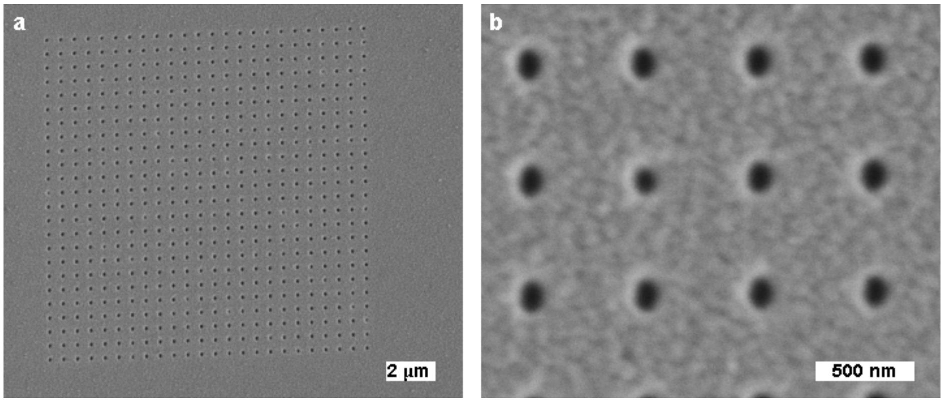

Figure 4.2 SEM images of the 578 nm periodicity subwavelength hole array: 8000 × magnification (a) and 65000 × magnification (b).

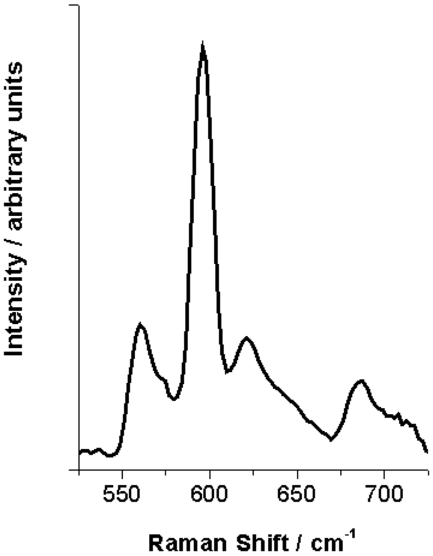

Figure 4.3 The (baseline-corrected) SERS spectrum of oxazine 720 on nanoholes in copper. The spectrum shown here was acquired from the 578 nm periodicity array using a forward-scattering geometry.

An average and a standard deviation were calculated for the 596 cm^{-1} band intensities obtained from each array. Array size and laser spot diameter were constant in our experiments; therefore, as hole-periodicity increases the number of scattering centers probed must decrease. Our data was normalized to account for this: average SERS intensity was divided by the number of holes in the array. These normalized average intensity values are plotted against hole-periodicity in Figure 4.4. Normalized standard deviation values are shown as error bars.

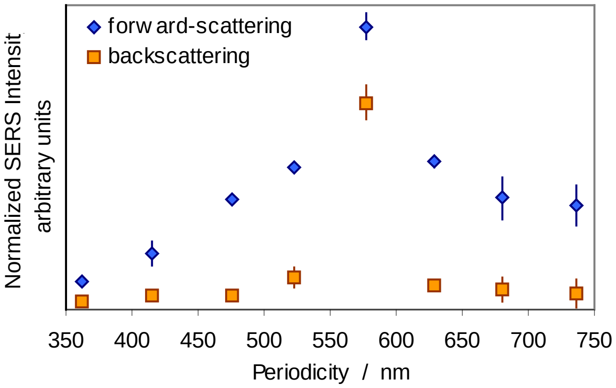

Figure 4.4 Normalized SERS intensity plotted as a function of each array's inter-hole distance (hole-periodicity).

An absolute enhancement factor cannot be calculated for oxazine 720 because ordinary Raman scattering from this dye is overwhelmed by its fluorescence when a 633 nm excitation source is used. However, a relative enhancement factor may be calculated if the ordinary Raman signal of some other compound is used as a reference. The ordinary Raman spectrum of benzene was obtained from a backscattering geometry experiment similar to the one employed for oxazine 720; except a smooth surface was used to eliminate the possibility of SERS, and a greater sample volume was used to obtain a reasonably strong signal (benzene depth was approximately equal to the focal length of an Olympus MS Plan 50 × ultra-long working distance microscope objective). We estimated an enhancement factor of 1×10^4 for the 596 cm^{-1} band of oxazine 720, relative to the ring-breathing band of benzene, for the 578 nm periodicity array in the backscattering geometry (see Appendix A for the calculation). We note that this enhancement factor contains a resonance-Raman component as well as the SERS component, and that the resonance Raman contribution may range from a factor of 10 to 10^3. The lack of signal from oxazine 720 on the unpatterned copper surface shows the SERS contribution is essential to overcome the detection limit of our system.

Rowlen et al suggested that metal-surface graininess made an important contribution to the enhancement they observed from benzenethiol adsorbed on nanoholes in a silver film.[17] Enhancement from graininess was not evident in the copper film investigated here, as graininess did not allow observation of SERS in the absence of nanohole arrays.

Figure 4.4 shows that for both experimental geometries, the 578 nm periodicity array gave the most intense SERS signal. In the following discussion, we show that this result can be rationalized using the simplified relationship between SP wavelength and hole-periodicity given by Equation 4.1, as well as rigorous numerical calculations performed using the FDTD method. In the latter case, electric field intensity perpendicular to the surface of the nanostructured metal was determined for each periodicity in each experimental geometry.

At normal incidence, an approximated relationship between SP resonance wavelength, λ, and hole-periodicity, p, for a square array of nanoholes is given by

$$(i^2 + j^2)^{1/2} \lambda = p\left(\frac{\varepsilon_1 \varepsilon_2}{\varepsilon_1 + \varepsilon_2}\right)^{1/2} \qquad (4.1)$$

where ε_1 is the permittivity of the metal, ε_2 is the permittivity of the dielectric in contact with the metal, and *i* and *j* are scattering orders for the array.[25] We will use the excitation wavelength, $\lambda = 633$ nm, to determine resonant periodicity because in our case λ is fixed and *p* is variable.

The real part of the permittivity of the metal is calculated from its index of refraction, *n*, and its extinction coefficient, *k*, using

$$\varepsilon_1 = n^2 - k^2 \qquad (4.2)$$

where *n* and *k* are wavelength dependent. The values published by Johnson and Christy for copper at a wavelength closest to 633 nm are $n = 0.30$ and $k = 3.205$.[24] Using these values in Equation 4.2 yields $\varepsilon_1 = -10.2$. Now $\varepsilon_2 = 1$ for air, and if $(i^2 + j^2)^{1/2} = 1$, then Equation 4.1 predicts that a periodicity of 601 nm will be in resonance with SPs produced on a copper surface by a He-Ne laser.

It is known, however, that *p* values calculated using Equation 4.1 will in general be about 4 % greater than experimental ones.[29] This is because Equation 4.1 does not take into account losses that arise from scattering by the holes,[29] or changes in the effective values of ε_1 and ε_2 at the interface ("n'_{eff}" in reference 3) caused by coupling through the holes.[3] After a 4 % correction, the predicted resonant periodicity becomes 578 nm; and indeed this array was found to give the greatest SERS intensity.

The eight nanohole arrays used in this work were also modelled using FDTD. In Figure 4.5, contours map electric fieldstrength perpendicular to the surface, $|Ez|^2$, at a height of 5 nm above the surface of the 578 nm periodicity array. The backscattering experiment was modeled to obtain Figure 4.5a and the forward-scattering experiment was modeled to obtain Figure 4.5b.

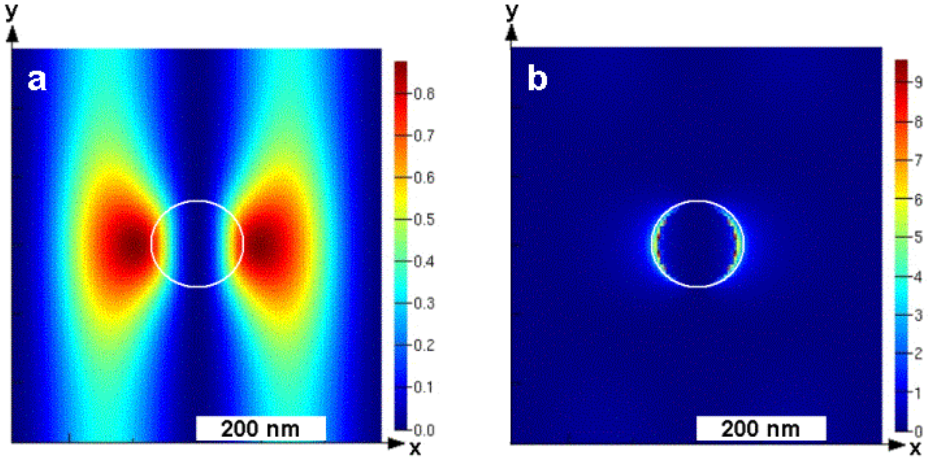

Figure 4.5 Field distribution contours surrounding a hole (centre of the picture) within the 578 nm periodicity array are shown for the backscattering geometry (a) and the forward-scattering geometry (b). Polarization of the incident beam is parallel to the x-axis.

The maximum $|Ez|^2$ value obtained for each array in the backscattering geometry was squared (because in a first approximation, SERS intensity is proportional to $|Ez|^4$ [30]) and plotted against hole-periodicity to produce the FDTD results shown in Figure 4.6. It can be seen, when this FDTD data (triangles) is overlaid with experimental data from Figure 4.4 (squares), that maximum $|Ez|^4$ field intensity and SERS intensity plots for the backscattering geometry are almost identical. This is true for both the overall shape of the plots and the position of the maximum, which occurs for the 578 nm periodicity array.

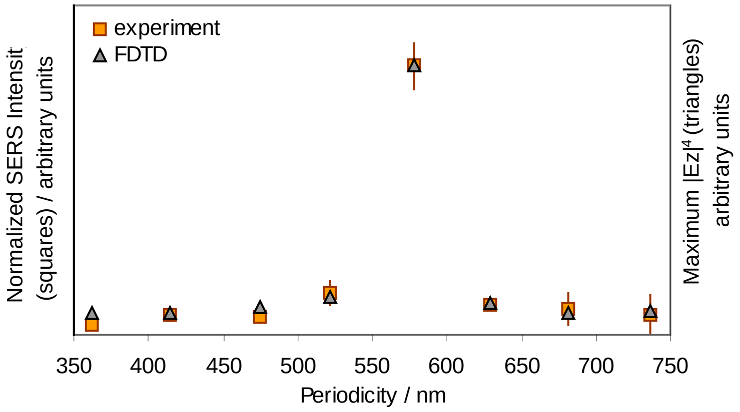

Figure 4.6 Maximum $|Ez|^4$ data, overlaid with SERS intensity data, for the backscattering geometry.

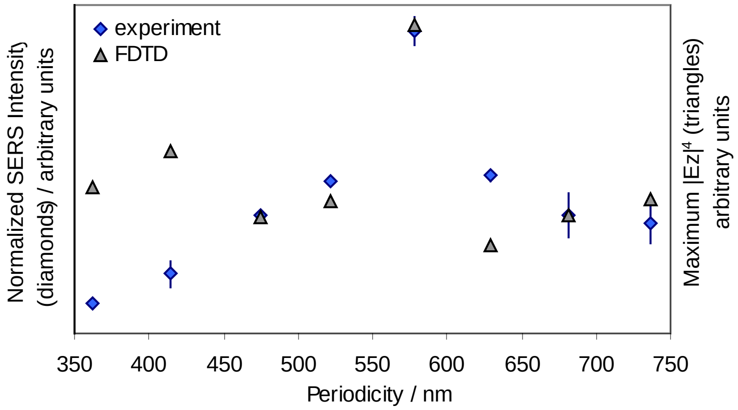

Figure 4.7 Maximum $|Ez|^4$ data, overlaid with SERS intensity data, for the forward-scattering geometry.

Figure 4.7 is the forward-scattering analogue of Figure 4.6. The position of the experimental maximum given in Figure 4.4 (i.e., the 578 nm periodicity array) was again reproduced by calculation; however, the overall shape of the forward-scattering plot was not reproduced as well as the overall shape of the backscattering plot. The reason for the discrepancy is not known. Apparently, some aspect of the forward-scattering experiment was not captured by the model. For instance there may be some inaccuracy from the material model used for the chromium adhesion layer, and this could have a greater effect on the forward-scattering simulations than on the backscattering ones. We wish to emphasize that when the forward-scattering experiment was modelled using FDTD, the 578 nm periodicity array yielded the greatest value for maximum field intensity and this result is consistent with our experimental SERS data.

Hitherto we have discussed only FDTD results for electric fieldstrength perpendicular to the surface, $|Ez|^2$, because SERS intensity is primarily dependent upon this quantity. Electric and magnetic fieldstrength parallel to the surface, $|Ex|^2$ and $|Hy|^2$, were also modeled for both geometries; and in each of these four data sets, the 578 nm periodicity array yielded the greatest value for maximum field intensity. Fieldstrength contour maps for $|Ex|^2$ and $|Hy|^2$, obtained by modeling the 578 nm periodicity array, are provided in Appendix A. Under certain conditions, electric field parallel to the surface may contribute to SERS intensity.[31] Magnetic fields cannot contribute to SERS intensity, however it is interesting to see how $|Hy|^2$ compares with $|Ez|^2$ and $|Ex|^2$.

Although areas of no field (dark blue regions) flank Figure 4.5a and surround the hole in Figure 4.5b, FDTD calculations clearly indicate that between-hole coupling does occur because intensity and contour results vary with periodicity. This is true for each of the other four data sets as well: $|Ex|^2$ and $|Hy|^2$ in the forward and backscattering geometries.

4.4 Conclusions

In this chapter, we showed that an array of subwavelength holes in copper may be used as a substrate for SERS. SP effects in copper are of interest because copper is abundantly present on earth, and may therefore provide a cheaper alternative to silver and gold which are normally used for SP-based optical devices.

Calculations were performed using a simplified relationship[25] between SP resonance wavelength and hole-periodicity, as well as the more rigorous FDTD method. Both levels of theory predicted the periodicity of maximum SERS intensity that was observed experimentally. Thus, we demonstrated that these two methods are consistent with each other and with experiment for the copper substrates used in this chapter.

4.5 References and Notes

1. Ebbesen TW, Lezec HJ, Ghaemi HF, Thio T, Wolff PA **1998** Extraordinary Optical Transmission Through Sub-Wavelength Hole Arrays *Nature* 391, 667-669
2. Barnes WL, Dereux A, Ebbesen TW **2003** Surface Plasmon Subwavelength Optics *Nature* 424, 824-830
3. Coe JV, Heer JM, Teeters-Kennedy S, Tian H, Rodriguez KR **2008** Extraordinary Transmission of Metal Films with Arrays of Subwavelength Holes *Annu. Rev. Phys. Chem.* 59, 179-202
4. Genet C, Ebbesen TW **2007** Light in Tiny Holes *Nature* 445, 39-46
5. Raether H **1988** *Surface Plasmons on Smooth and Rough Surfaces and on Gratings* Springer-Verlag, Berlin
6. Martín-Moreno L, García-Vidal FJ, Lezec HJ, Pellerin KM, Thio T, Pendry JB, Ebbesen TW **2001** Theory of Extraordinary Optical Transmission Through Subwavelength Hole Arrays *Phys. Rev. Lett.* 86, 6, 1114-1117
7. Liu H, Lalanne P **2008** Microscopic Theory of the Extraordinary Optical Transmission *Nature* 452, 728-731
8. Dintinger J, Degiron A, Ebbesen TW **2005** Enhanced Light Transmission Through Subwavelength Holes *MRS Bull.* 30, 381-384
9. Srituravanich W, Fang N, Sun C, Luo Q, Zhang X **2004** Plasmonic Nanolithography *Nano Lett.* 4, 6, 1085-1088

10. Liu C, Kamaev V, Vardeny ZV **2005** Efficiency Enhancement of an Organic Light-Emitting Diode with a Cathode Forming Two-Dimensional Periodic Hole Array *Appl. Phys. Lett.* 86, 143501

11. Gordon R, Sinton D, Kavanagh KL, Brolo AG **2008** A New Generation of Sensors Based on Extraordinary Optical Transmission *Acc. Chem. Res.* 41, 8, 1049-1057

12. Leebeeck AD, Kumar LKS, Lange Vd, Sinton D, Gordon R, Brolo AG **2007** On-Chip Surface-Based Detection with Nanohole Arrays *Anal. Chem.* 79, 4094-4100

13. Liu Y, Bishop J, Williams L, Blair S, Herron J **2004** Biosensing Based Upon Molecular Confinement in Metallic Nanocavity Arrays *Nanotechnology* 15, 1368-1374

14. Pang L, Hwang GM, Slutsky B, Fainman Y **2007** Spectral Sensitivity of Two-Dimensional Nanohole Array Surface Plasmon Polariton Resonance Sensor *Appl. Phys. Lett.* 91, 123112

15. Stark PRH, Halleck AE, Larson DN **2005** Short Order Nanohole Arrays in Metals for Highly Sensitive Probing of Local Indices of Refraction as the Basis for a Highly Multiplexed Biosensor Technology *Methods* 37, 37-47

16. Brolo AG, Arctander E, Gordon R, Leathem B, Kavanagh KL **2004** Nanohole-Enhanced Raman Scattering *Nano Lett.* 4, 2015-2018

17. Thomas H. Reilly I, Chang S-H, Corbman JD, Schatz GC, Rowlen KL **2007** Quantitative Evaluation of Plasmon Enhanced Raman Scattering from Nanoaperture Arrays *J. Phys. Chem. C* 111, 1689-1694

18. Thomas H. Reilly I, Corbman JD, Rowlen KL **2007** Vapor Deposition Method for Sensitivity Studies on Engineered Surface-Enhanced Raman Scattering-Active Substrates *Anal. Chem.* 79, 5078-5081

19. Yu Q, Golden G **2007** Probing the Protein Orientation on Charged Self-Assembled Monolayers on Gold Nanohole Arrays by SERS *Langmuir* 23, 8659-8662

20. Yu Q, Guan P, Qin D, Golden G, Wallace PM **2008** Inverted Size-Dependence of Surface-Enhanced Raman Scattering on Gold Nanohole and Nanodisk Arrays *Nano Lett.* 8, 1923-1928

21. Williams SM, Rodriguez KR, Teeters-Kennedy S, Shah S, Rogers TM, Stafford AD, Coe JV **2004** Scaffolding for Nanotechnology: Extraordinary Infrared Transmission of Metal Microarrays for Stacked Sensors and Surface Spectroscopy *Nanotechnology* 15, S495-S503
22. Williams SM, Rodriguez KR, Teeters-Kennedy S, Stafford AD, Bishop SR, Lincoln UK, Coe JV **2004** Use of the Extraordinary Infrared Transmission of Metallic Subwavelength Arrays to Study the Catalyzed Reaction of Methanol to Formaldehyde on Copper Oxide *J. Phys. Chem. B* 108, 11833-11837
23. Przybilla F, Degiron A, Laluet J-Y, Genet C, Ebbesen TW **2006** Optical Transmission in Perforated Noble and Transition Metal Films *J. Opt. A Pure Appl. Opt.* 8, 458-463
24. Johnson PB, Christy RW **1972** Optical Constants of the Noble Metals *Phys. Rev. B* 6, 12, 4370-4379
25. Ghaemi HF, Thio T, Grupp DE **1998** Surface Plasmons Enhance Optical Transmission Through Subwavelength Holes *Phys. Rev. B* 58, 11, 6779-6782
26. Gordon R, Hughes M, Leathem B, Kavanagh KL, Brolo AG **2005** Basis and Lattice Polarization Mechanisms for Light Transmission Through Nanohole Arrays in a Metal Film *Nano Lett.* 5, 1243-1246
27. Lide DR, ed. **1995** *CRC Handbook of Chemistry and Physics, 76th Edition* p. 12.128 CRC Press, Boca Raton
28. Brolo AG, Sanderson AC **2004** Surface-Enhanced Raman Scattering (SERS) from a Silver Electrode Modified with Oxazine 720 *Can. J. Chem.* 82, 1474-1480
29. Genet C, van Exter MP, Woerdman JP **2003** Fano-Type Interpretation of Red Shifts and Red Tails in Hole Array Transmission Spectra *Opt. Commun.* 225, 331-336
30. Moskovits M **2005** Surface-Enhanced Raman Spectroscopy: A Brief Retrospective *J. Raman Spectrosc.* 36, 485-496
31. Moskovits M, Suh JS **1984** Surface Selection Rules for Surface-Enhanced Raman Spectroscopy: Calculations and Application to the Surface-Enhanced Raman Spectrum of Phthalazine on Silver *J. Phys. Chem.* 88, 5526-5530

Chapter 5: Nanoscale Gratings in a Gold Film

5.1 Introduction

This chapter links Chapter 3 and Chapter 4: we use the methods of Chapter 4 to continue exploring the SERS substrate of Chapter 3. Herein we study SERS from focused ion beam (FIB) milled gratings in a gold film. We vary the width of the grooves and the width of the metal lines between them, and we examine the resulting effect on SERS intensity (I_{SERS}) in the backscattering and forward-scattering geometries.

Many authors have studied SERS from gratings[1-21] (we note that the scratches described in Chapter 3 may also be considered gratings). Several reports[8-10,20,21] show the effect of periodicity on SERS intensity, and most of these[8-10,20] explore different groove/line widths for one or more constant periodicities. References 8 to 10, 20 and 21 are summarized below: relevant figures will be highlighted, and the overall relevance of each work to the current study will be assessed.

Kahl, Voges and Hill report the fabrication of gratings with systematically varied periodicities, groove widths and line widths for use as SERS substrates in a 1998 *Spectroscopy Europe* article.[9] However, the focus of the article is on raising awareness for the procedure used - electron beam lithography. SERS data for the different groove/line width combinations is not presented, nor are optimal grating dimensions given. The authors say that enhancement increases as grating periodicity decreases from 800 to 200 nm; but groove width, line width, and even the type of metal (silver, gold or copper) are unspecified.

In the same year, Kahl et al published a more technical paper providing additional information.[10] Although ≥ 83 different gratings with various periodicities and various groove/line width combinations were made, I_{SERS} data is presented for only 19 of them (Figures 7 and 8 in reference 10, reproductions are provided in Appendix B of the present work). Only 2 of the ≥ 83 gratings match ours with respect to periodicity and groove/line width, so the lack of I_{SERS} data presented in reference 10 is of little consequence to us. Furthermore, they used a silver metal-depth of 40 nm whereas we used a gold metal-depth of 100 nm.

Kahl and Voges later carried out a comprehensive theoretical study detailing the effect of various parameters on the SERS enhancement factor (EF): angle of incidence, detection angle, grating depth, grating periodicity, and various groove/line width combinations for a constant periodicity.[8] In Figure 9 of reference 8 (Figure 5.1 below[22]), EF is plotted against depth for five silver gratings having different *line width / period* ratios. Here, groove width decreases as line width increases, and periodicity remains constant at 600 nm. Where comparable (same depth, same periodicity, same or similar *line width / period* ratio), their data agrees qualitatively with the forward-scattering I_{SERS} data presented in this chapter; the agreement will be discussed further in section 5.3.

Wirgin and Maradudin examined SERS from gratings with incident light polarized along the grooves and the lines.[20] This kind of study is unusual because a cross-grating polarization is needed to acquire strong signal. Wirgin and Maradudin show the effect of simultaneously changing periodicity and line width on resonant enhancement (i.e., enhancement optimized with respect to wavelength) in Figure 28, which is reproduced in Appendix B. They plot the effect of wavelength on enhancement for various groove/line widths (periodicity remains constant at 400 nm) in Figures 29 to 31, which are also reproduced in Appendix B. However, all of the theoretical gratings described by Figures 28 to 31 have a width (groove or line) that differs from our corresponding width by 50 nm or more. They have a depth of 1000 nm, and they are perfectly conducting (their activity may approximate the activity of silver gratings at certain wavelengths). All things considered, it seems inappropriate to compare the results presented in reference 20 with our results.

Yamashita and Tsuji studied the effect of incident wavelength, grating depth, grating periodicity and type of metal on EF.[21] This seems to be the only report in which periodicity was varied, but groove/line widths for a given periodicity were not. Figure 3 in reference 21 (Figure 5.2 below[23]) shows the effect of incident wavelength on maximum EF (EF was optimized with respect to grating depth) for theoretical silver gratings having different periodicities. If groove and line widths were set equal to one another, the results presented in Figure 3 also match, qualitatively, our forward-scattering I_{SERS} data where comparable (in terms of periodicity and groove/line widths). Again, the agreement will be discussed further in section 5.3.

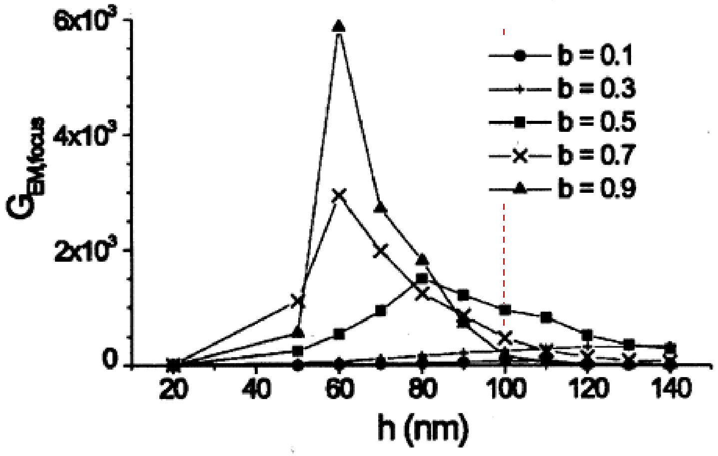

Figure 9 Enhancement factor plotted as a function of grating depth for different *line width / period* ratios (b-values). Period = 600 nm.

Figure 5.1 Figure 9 from Kahl and Voges, 2000, *Phys. Rev. B*, 61, 20, 14078-14088. Reproduced with permission.[22] The vertical, dashed red line marks our grating depth.

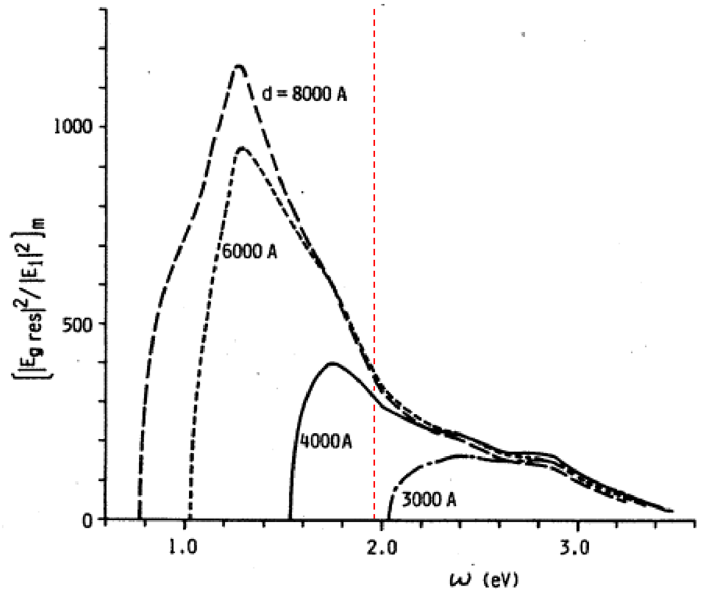

Figure 3 Enhancement factor, optimized with respect to grating depth, is plotted against incident light energy (it is the corresponding wavelength that is of interest to us) for different grating periods.

Figure 5.2 Figure 3 from Yamashita and Tsuji, 1983, *J. Phys. Soc. Jpn.*, 52, 7, 2462-2471. Reproduced with permission.[23] The vertical, dashed red line marks our incident light energy (wavelength).

5.2 Experimental Methods

Gratings were milled in a commercially available gold-plated glass slide from Evaporated Metal Films (EMF). This gold-plated glass slide was of the same type as the ones described in section 3.2: the gold film was 100 nm thick, and a 5 nm chromium layer was used to improve adhesion between the gold and the glass.

Gratings were milled using a focused ion beam (FIB) and imaged using a scanning electron microscope (SEM) by our collaborators Samantha Grist and Karen Kavanagh (Department of Physics at Simon Fraser University). We note that FIB milling and SEM imaging are the SERS-substrate preparation techniques of Chapter 4. The width of the grooves (g) were 150, 300 and 450 nm; the width of the metal lines between them (m) were 150, 300 and 450 nm. The nine combinations milled are given in Table 5.1. Grating periodicity (Λ) ranged from 300 to 900 nm.

Oxazine 720 was used as a probe molecule here, as in Chapter 3 and Chapter 4, because it has a very high cross-section. The gold-plated glass slide was tilted; three drops of 5.0 μM oxazine 720 in methanol were added to the surface and allowed to run down over the gratings; the sample was rinsed with plenty of ultrapure water (18.2 MΩ cm) from a Barnstead NANOpure Diamond water purification system; and finally, the surface was blown dry with 99.998 % pure nitrogen.

The backscattering and forward-scattering SERS setups used to examine nanoholes in copper (Figure 4.1) were also used to examine the gratings in gold. Acquisition time was 70 s for the backscattering geometry and 200 s for the forward-scattering geometry. SERS intensity measurements were double-checked by Mohammad Rahman (Department of Chemistry at the University of Victoria).

Table 5.1 Groove widths (g), metal line widths (m), and periodicities (Λ) for the gratings studied.

		Groove Width		
		150	300	450
Metal Line Width	150	g150m150 Λ300	g300m150 Λ450	g450m150 Λ600
	300	g150m300 Λ450	g300m300 Λ600	g450m300 Λ750
	450	g150m450 Λ600	g300m450 Λ750	g450m450 Λ900

5.3 Results and Discussion

Nine gratings (Table 5.1) were milled by FIB in a 100 nm gold film. The width of the grooves were 150, 300 and 450 nm; the width of the metal lines between them were 150, 300 and 450 nm. SEM images of the g150m150 and g450m450 gratings appear in Figure 5.3. Oxazine 720 was added to the surface for use as a probe. SERS spectra were acquired in backscattering and forward-scattering experiments (Figure 4.1), with polarization of the incident beam across and along the gratings.

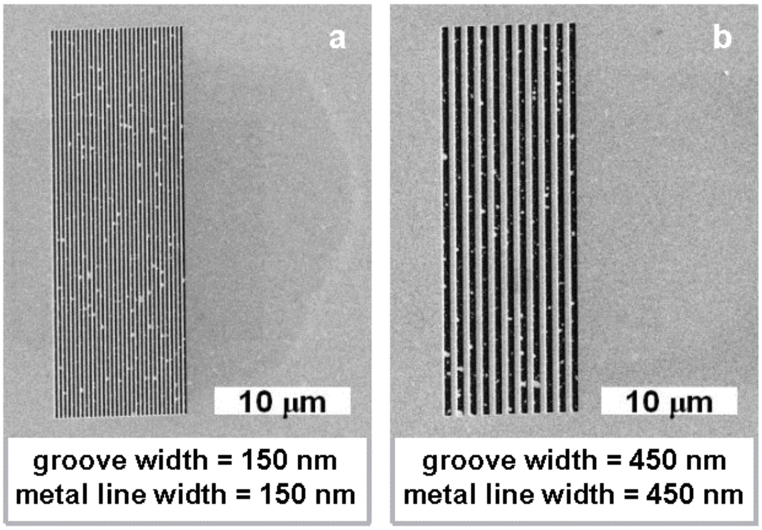

Figure 5.3 SEM images showing the g150m150 (a) and g450m450 (b) gratings. The specks in the grooves are fabrication defects.

SERS intensity, obtained with the incident light polarized across each grating, is plotted as a function of groove width and metal line width in Figure 5.4. When data from the backscattering (Figure 5.4a) and forward-scattering (Figure 5.4b) experiments are considered together, some trends become evident:

- When groove width is 150 nm, SERS intensity increases with line width.
- When groove width is 300 nm, the same trend is observed.
- When groove width is 450 nm, however, SERS intensity seems to peak when line width is 300 nm.
- When line width is 150 nm, SERS intensity is weak.
- When groove width is 150 nm, SERS intensity is diminished (relative to the other groove widths) on going from the backscattering to the forward-scattering experiment. I.e., the three 150 nm groove width bars are much higher for the backscattering experiment than they are for the forward-scattering experiment (relative to the other bars).

When the incident light was polarized along each grating, SERS intensity data showed no strong trends. We attribute this to a combination of two factors: weak SERS activity from the gratings in the parallel geometry, and SERS activity from the defects in the grooves (these defects can be seen in Figure 5.3).

Defects were also associated with the scratches, and may be seen at the edge of the scratch shown in Figure 3.1. Defects did not pose a problem in Chapter 3 because SERS intensity values that were compared directly always originated from the same scratched area. I.e., the set of defects remained constant because the polarization of the incident light was rotated within a particular scratched area during each experiment. Defects pose a greater problem in this chapter because we wish to study geometrical-parameter effects: we wish to make a direct comparison of SERS intensity values obtained from different gratings, however each grating has a different set of defects.

Since the parallel geometry SERS intensities showed no strong trends, $p_{observed}$ values (obtained using Equation 3.3) also showed no strong trends. We note that $p_{observed}$ values ranged from -0.2 to 0.4 in the backscattering geometry, and from -0.1 to 0.6 in the forward-scattering geometry. A value of $p_{observed} < 0$ means that, after correcting for polarization artifacts introduced by the microscope, SERS intensity was greater with the laser polarized along the grating than it was with the laser polarized across the grating.

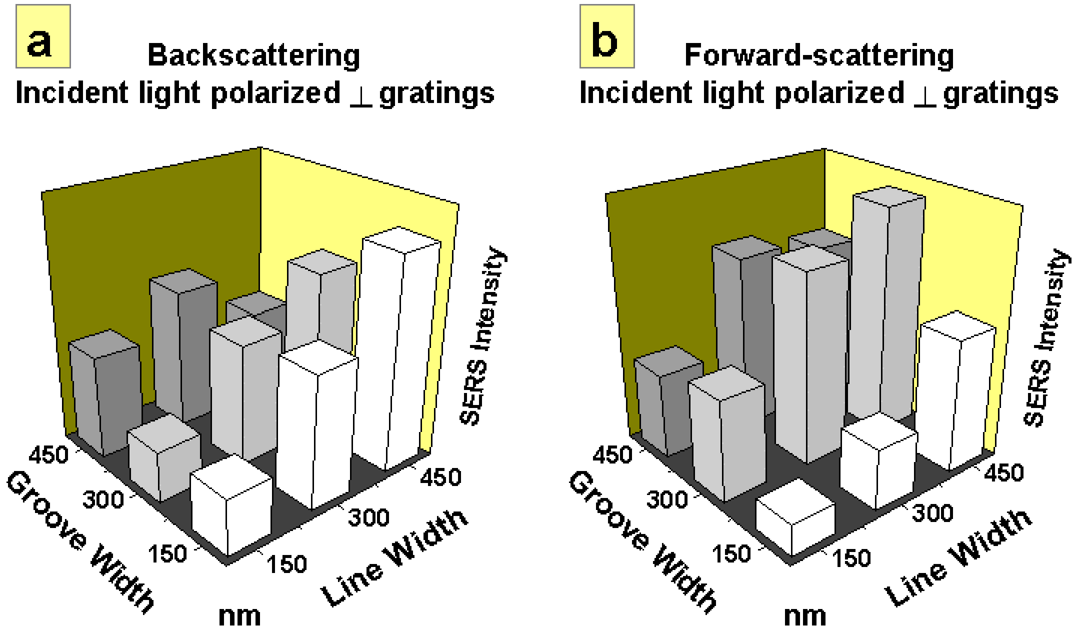

Figure 5.4 SERS intensity plotted as a function of groove width and metal line width.

In section 5.1 it was said that the forward-scattering I_{SERS} results presented in this chapter (Figure 5.4b) qualitatively match theoretical EF data published by Kahl and Voges.[8] They calculated electric near-fields using a Rayleigh expansion technique, and determined SERS EFs by applying the Lorentz reciprocity theorem. The qualitative agreement is seen when certain aspects of the two data types are comparable: same depth, same periodicity, same or similar groove/line width; and it is seen in spite of certain other differences: the nature of the samples (Figure 5.5) and the optical setup (their EF values were calculated for a backscattering geometry, our matching I_{SERS} values were measured in a forward-scattering experiment). In Figure 9 of reference 8 (Figure 5.1 in section 5.1[22]), EF is plotted against grating depth for five different *line width / period* ratios (the authors imply that all gratings have a 600 nm periodicity, and line width is the actual variable). For a 100 nm grating depth, line widths of 180, 300 and 420 nm yield EFs of approximately 240, 950 and 470 (Table 5.2, first column).[24] It is possible to compare these gratings with our g450m150, g300m300 and g150m450 gratings, all of which have a periodicity of 600 nm and a grating depth of 100 nm. With the forward-scattering experiment, we found that line-widths of 150, 300 and 450 nm yield I_{SERS} of 770, 1730 and 1200 counts (Table 5.2, second column). Table 5.2 shows that EF (first column) and I_{SERS} (second column) increase and then drop somewhat as line width increases from $150 \approx 180$ to 300 to $420 \approx 450$.

Figure 9 in Kahl and Voges, 2000, *Phys. Rev. B*, 61, 20, 14078-14088:
the entire structure is silver

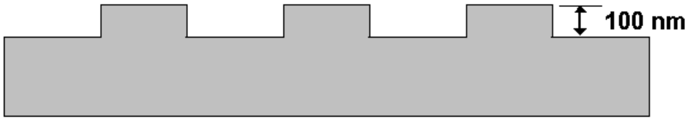

Present Work:
gold on a chromium adhesion layer, grooves were milled through the metal into the glass

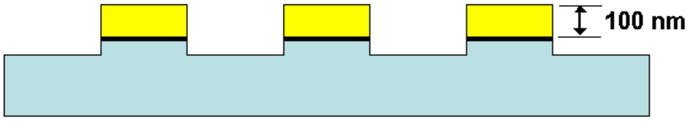

Figure 5.5 The grating-type modeled to obtain Figure 9 in reference 8 is compared to our grating-type.

Table 5.2 The data in Figure 9 of reference 8 is compared to the data we present in Figure 5.4b.

Figure 9 in Reference 8: line width (nm) and EF when periodicity = 600 nm and SERS metal depth = 100 nm	Figure 5.4b in the Present Work: line-width (nm) and I_{SERS} (counts) when periodicity = 600 nm and SERS metal depth = 100 nm
180 yields 240	150 yields 770
300 yields 950	300 yields 1730
420 yields 470	450 yields 1200

The forward-scattering I_{SERS} results presented in this chapter (Figure 5.4b) also agree qualitatively with theoretical EF results published by Yamashita and Tsuji.[21] They employed a perturbation theory based on that of Jha et al.[7] Figure 3 in reference 21 (Figure 5.2 in section 5.1[23]) shows the effect of incident wavelength on maximum EF (EF was optimized with respect to grating depth) for sinusoidal silver gratings having different periodicities. For a 300 nm periodicity, EF was calculated to be 0 for all wavelengths greater than 608 nm (all energies less than 2.04 eV). The wavelength that we used was 633 nm (1.96 eV), which lies on the 0 side but close to the cutoff. At our wavelength (or energy), Figure 3 in reference 21 shows that 400, 600 and 800 nm periodicities yield significant EFs that are similar to one another. It may be seen in Figure 5.4b of the present work that when groove and line widths are equal, and when periodicity is 300 nm, I_{SERS} is low. When groove and line widths are equal and when periodicity is 600 or 900 nm, I_{SERS} values are much greater and they are similar to one another.

5.4 Conclusions and Future Work

SERS from oxazine 720 on nine gratings with different groove/line width combinations, milled by FIB in a film of gold, was observed in backscattering and forward-scattering experiments.

Some trends in I_{SERS} ($\equiv I_{\perp}$) were seen when the incident light was polarized across the gratings. No strong trends in I_{SERS} ($\equiv I_{//}$) were seen when incident light was polarized along the gratings; hence none were seen in $p_{observed}$. The forward-scattering data in Figure 5.4b agrees qualitatively with the literature where comparable.

We plan to obtain finite-difference time-domain (FDTD) results, for our gratings specifically, by collaboration.

5.5 References and Notes

1. Baltog I, Primeau N, Reinisch R, Coutaz JL **1995** Surface Enhanced Raman Scattering on Silver Grating: Optimized Antennalike Gain of the Stokes Signal of 10^4 *Appl. Phys. Lett.* 66, 10, 1187-1189
2. Duschl C, Knoll W **1988** Structural Characterization of Langmuir-Blodgett Multilayer Assemblies by Plasmon Surface Polariton Field-Enahnced Raman Spectroscopy *J. Chem. Phys.* 88, 6, 4062-4069

3. Fujimaki H, Suzuki Y, Hatta A **1994** Enhanced Raman Scattering from Silver Metal Gratings Coated with p-Nitrobenzioc Acid Films *J. Raman Spectrosc.* 25, 303-306
4. Garcia N **1983** Exact Calculations of Scattering and Enhanced Fields of Electromagnetic Waves on Grating Surfaces *J. Electron Spectrosc.* 29, 421-425
5. Girlando A, II JGG, Heitmann D, Philpott MR, Seki H, Swalen JD **1980** Raman Spectra of Molecules on Metal Surfaces *Surf. Sci.* 101, 417-424
6. Girlando A, Philpott MR, Heitmann D, Swalen JD, Santo R **1980** Raman Spectra of Thin Organic Films Enhanced by Plasmon Surface Polaritons on Holographic Metal Gratings *J. Chem. Phys.* 72, 9, 5187-5191
7. Jha SS, Kirtley JR, Tsang JC **1980** Intensity of Raman Scattering from Molecules Adsorbed on a Metallic Grating *Phys. Rev. B* 22, 8, 3973-3982
8. Kahl M, Voges E **2000** Analysis of Plasmon Resonance and Surface-Enhanced Raman Scattering on Periodic Silver Structures *Phys. Rev. B* 61, 20, 14078-14088
9. Kahl M, Voges E, Hill W **1998** Optimisation of SERS Substrates by Electron-Beam Lithography *Spectrosc. Eur.* 10, 6, 8-13
10. Kahl M, Voges E, Kostrewa S, Viets C, Hill W **1998** Periodically Structured Metallic Substrates for SERS *Sensor Actuat. B Chem.* 51, 285-291
11. Knoll W, Philpott MR, Swalen JD, Girlando A **1982** Surface Plasmon Enhanced Raman Spectra of Monolayer Assemblies *J. Chem. Phys.* 77, 5, 2254-2260
12. Kocabas A, Ertas G, Senlik SS, Aydinli A **2008** Plasmonic Band Gap Structures for Surface-Enhanced Raman Scattering *Opt. Express* 16, 17, 12469-12477
13. Mrozek I, Otto A **1990** Quantitative Separation of the "Classical" Electromagnetic and the "Chemical" Contribution to Surface Enhanced Raman Scattering *J. Electron Spectrosc.* 54, 55, 895-911
14. Nevière M, Reinisch R **1982** Electromagnetic Study of the Surface-Plasmon-Resonance Contribution to Surface-Enhanced Raman Scattering *Phys. Rev. B* 26, 10, 5403-5408

15. Nikitin PI, Beloglazov AA, Valeiko MV, Creighton JA, Smith AM, Sommerdijk NAJM, Wright JD **1997** Silicon-Based Surface Plasmon Resonance Chemical Sensors *Sensor Actuat. B Chem.* 38, 53-57
16. Nikitin PI, Beloglazov AA, Valeiko MV, Creighton JA, Wright JD **1997** Silicon-Based Surface Plasmon Resonance Combined with Surface-Enhanced Raman Scattering for Chemical Sensing *Rev. Sci. Instrum.* 68, 6, 2554-2557
17. Numata H **1982** Contribution to SERS of Surface Plasmon Polariton Modes on Sinusoidal Metal Surface *J. Phys. Soc. Jpn.* 51, 8, 2575-2581
18. Tsang JC, Kirtley JR, Bradley JA **1979** Surface-Enhanced Raman Spectroscopy and Surface Plasmons *Phys. Rev. Lett.* 43, 11, 772-775
19. Tsang JC, Kirtley JR, Theis TN **1980** Surface Plasmon Polariton Contributions to Stokes Emission from Molecular Monolayers on Periodic Ag Surfaces *Solid State Comm.* 35, 667-670
20. Wirgin A, Maradudin AA **1986** Resonant Response of a Bare Metallic Grating to s-Polarized Light *Prog. Surf. Sci.* 22, 1, 1-99
21. Yamashita M, Tsuji M **1983** Simple Theory for Surface-Plasmon-Polariton Resonance on Sinusoidal Metal Surface: Application to SERS *J. Phys. Soc. Jpn.* 52, 7, 2462-2471
22. Reprinted, with permission, from *Phys. Rev. B*, 2000, 61, 20, 14078-14088. Kahl M, Voges E; Analysis of Plasmon Resonance and Surface-Enhanced Raman Scattering on Periodic Silver Structures. Copyright, 2000, American Physical Society.
23. Reprinted, with permission, from *J. Phys. Soc. Jpn.*, 1983, 52, 7, 2462-2471. Yamashita M, Tsuji M; Simple Theory for Surface-Plasmon-Polariton Resonance on Sinusoidal Metal Surface: Application to SERS. Copyright, 1983, Physical Society of Japan.
24. Enhancement factors were read off the graph. Line widths were obtained by multiplying the *line width / period* ratio, b, by a 600 nm periodicity.

Chapter 6: Concluding Remarks

6.1 Thesis Summary

In this work, progressively more ordered SERS substrates were examined.

We began with a look at SERS from polystyrene on gold clusters (a very simple substrate). The relationship that we observed between sample preparation parameters and gold-cluster morphology, and the one we observed between gold-cluster morphology and SERS intensity, are both consistent with the literature. The relationship that we observed between sample preparation parameters and SERS intensity, however, was unexpected. Vibrations were assigned to all bands between 250 and 1750 cm^{-1} in the ordinary Raman and SERS spectra of polystyrene (Table 2.1). We determined that polystyrene's phenyl ring is tilted with respect to the surface of the gold in our samples. It has been suggested that reactions involving silver catalyze polystyrene degradation during SERS; however, our results suggest that heating of the substrate is sufficient to cause uncatalyzed degradation.

We then explored polarization effects associated with unidirectional scratches in gold films. We introduced a way to quantify the extent of a polarization effect that takes into account polarization artefacts from the microscope used in Raman microscopy (Equation 3.3). We showed that polarization effects can be used to eliminate solution-phase interference signals from the SERS spectrum of an adsorbed analyte (Equation 3.4), and after demonstrating proof of concept, we used our technique to monitor the electrochemically-driven desorption and readsorption of cysteine.

Finally, precision milling allowed us to study the effect of periodicity on SERS from nanohole arrays in a copper film and the effect of groove/line width on SERS from nanoscale gratings in a gold film. For nanohole arrays in a copper film, our experimental and finite-difference time-domain (FDTD) results agree on the periodicity of maximum SERS intensity for both the forward and backscattering geometries. For nanoscale gratings in a gold film, our experimental forward-scattering results qualitatively match theoretical backscattering results presented in the literature. The work on nanoscale gratings is still in progress, and we intend to carry out FDTD modeling on these structures.

6.2 Overarching Conclusion

It may be said of the SERS substrates studied in this work that the potential for use increases with increasing order.

The gold clusters and gold-cluster aggregates of Chapter 2 are inhomogeneous, and the resulting SERS intensity is quite variable (as seen by comparing the red curves with the blue curves in Figure 2.1a, Figure 2.1b and Figure 2.2a).

The unidirectional scratches of Chapter 3 yield a polarization effect, and this effect may be used to eliminate solution-phase signals from the spectrum of an adsorbed analyte (Figure 3.6 and Figure 3.9).

The nanohole arrays of Chapter 4 were precision milled and possess order in two dimensions. SERS intensities obtained from these structures are reproducible (the error bars in Figure 4.4 are relatively small), and relative SERS intensities from these structures can be determined by FDTD when the appropriate input parameters are used

(Figure 4.6). We therefore assert that our nanohole arrays are a "controlled" SERS substrate.

We believe that if the nanoscale gratings of Chapter 5 had been milled without defect, experimental and FDTD results would match as well as they did for the nanohole arrays. Furthermore, a $p_{observed}$ value of ~ 0.4 is considered large for scratches in gold (Figure 3.7 and Figure 3.8), but (reliable) values closer to 1 are expected from (defect-free) gratings of the right geometry for surface plasmon (SP) resonance.

6.3 Outlook

Last year, ~ 1000 papers that study or use SERS were published; and the number of such papers published per annum is increasing exponentially.[1] SERS' close association with the field of plasmonics, and it's great potential for ultra-trace analysis and the monitoring of single molecules, are largely responsible for this rapid growth.

The continued development of nanofabrication techniques will yield greater control over hotspots, and more reliable SERS signals. The continued study of single-molecule SERS will yield new insights into the physical and chemical principles that underlie the behaviour of individual molecules, metal-molecule interactions, and related spectroscopic effects. Such progress will make SERS more accessible and more powerful, thus adding more breadth and more depth to its appeal. We therefore anticipate an exceptionally bright future for this extraordinarily bright scattering effect.

6.4 References and Notes

1. Graham D, Goodacre R **2008** Chemical and Bioanalytical Applications of Surface Enhanced Raman Scattering Spectroscopy *Chem. Soc. Rev.* 37, 883-884

Appendix A: Supplemental Data

Supplemental Data for Polystyrene on Gold Clusters (Chapter 2):

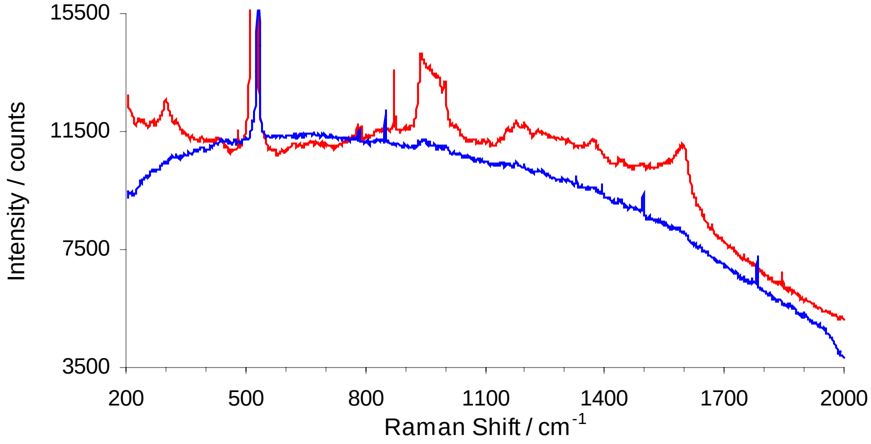

Spectra showing intermediate (red curve) and weak (blue curve) SERS obtained from the low current sample: gold was evaporated using 77.3 mA for 30 s/layer. Acquisition time for both spectra was 600 s. Cosmic rays were not removed, and these spectra were not baseline-corrected; they constitute the raw data presented in Figure 2.1a and Figure 2.1b.

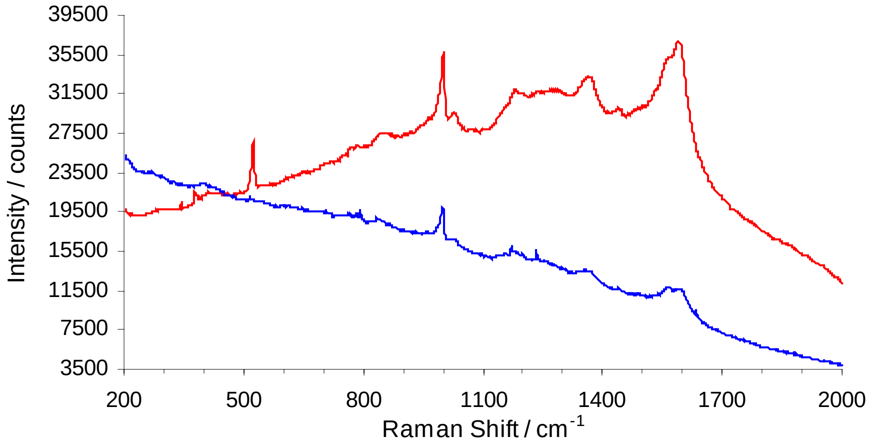

Spectra showing strong (red curve, acquisition time was 300 s) and intermediate (blue curve, acquisition time was 600 s) SERS obtained from the high current sample: gold was evaporated using 83.3 mA for 30 s/layer. Acquisition time was shortened for the spectrum showing strong SERS to prevent saturation of the detector and flat-topping of the most intense peaks. Cosmic rays were not removed, and these spectra were not baseline-corrected; they constitute the raw data presented in Figure 2.2a.

Supplemental Data for Scratched Gold Films (Chapter 3):

The Data Presented Graphically in Figure 3.2c

Scratch Orientation a (diamonds)		Scratch Orientation b (squares)	
Rotation of Incident-Beam Polarization, as Defined in Figure 3.2b (degrees)	Intensity of the 596 cm^{-1} band of oxazine 720 (arbitrary units)	Rotation of Incident-Beam Polarization, as Defined in Figure 3.2b (degrees)	Intensity of the 596 cm^{-1} band of oxazine 720 (arbitrary units)
0	3627	0	256
20	3966	20	481
40	3732	40	1608
60	2682	60	2762
80	1599	80	4123
100	834	100	4623
120	846	120	4484
140	1686	140	3218
160	2820	160	1819
180	3954	180	402
200	4167	200	519
220	3771	220	1862
240	2385	240	3709
260	1167	260	5374
280	564	280	6111
300	816	300	5335
320	1929	320	3570
340	3222	340	1489
360	3861	360	329

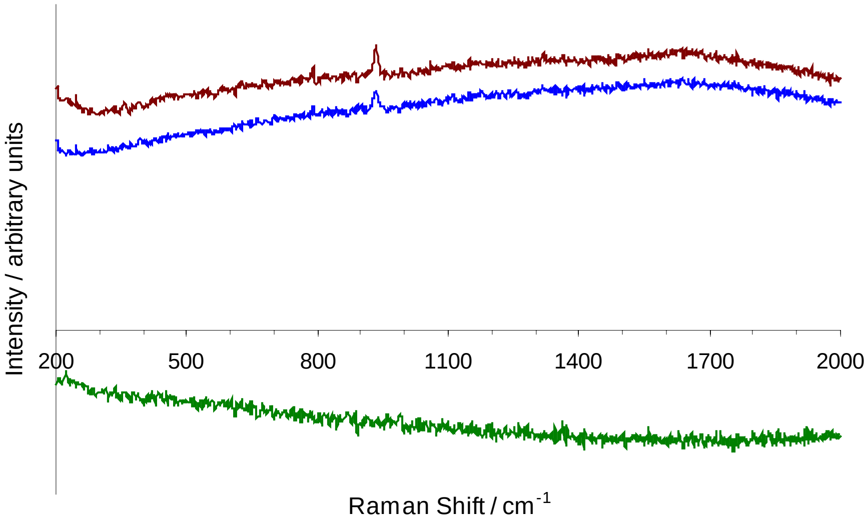

$S_\perp$ (red), $S_{//}$ (blue) and $S_{analytical}$ (green) for perchlorate. Acquisition time was 45 s. $S_\perp$ and $S_{//}$ were not baseline-corrected. These spectra constitute the raw data presented in Figure 3.4 and Figure 3.6a.

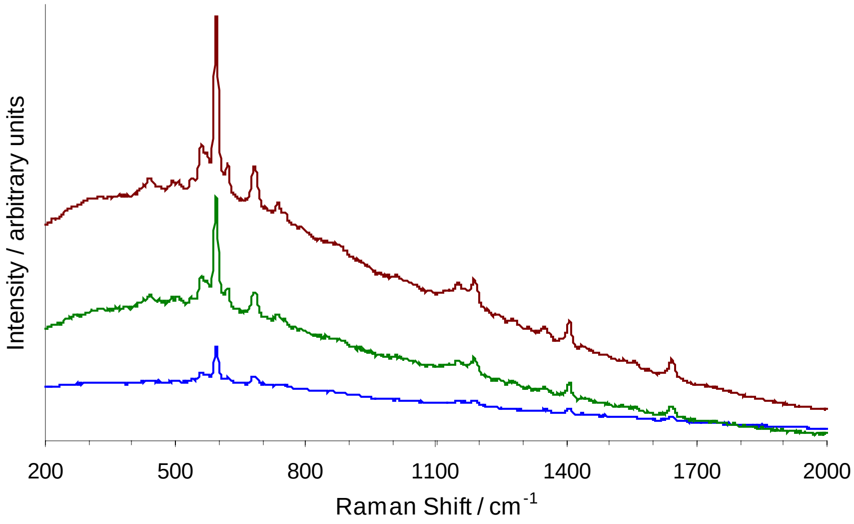

$S_\perp$ (red), $S_{//}$ (blue) and $S_{analytical}$ (green) for oxazine 720. Acquisition time was 20 s. $S_\perp$ and $S_{//}$ were not baseline-corrected. These spectra constitute the raw data presented in Figure 3.5 and Figure 3.6b.

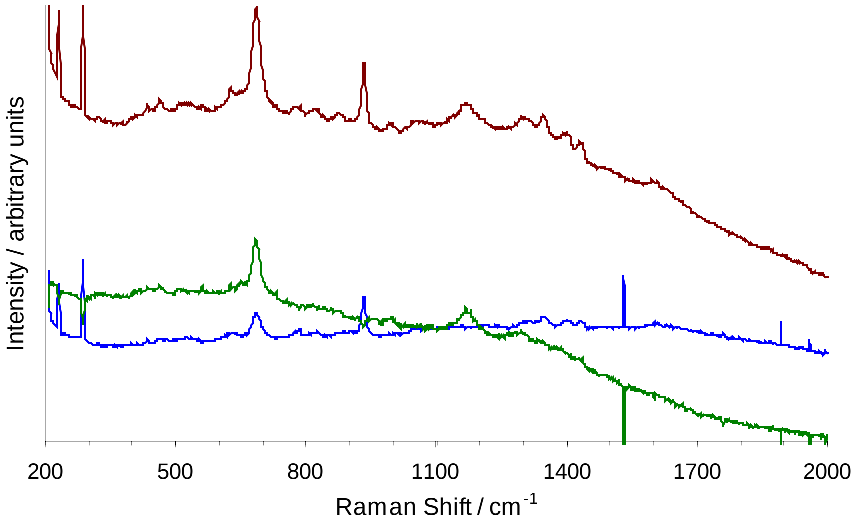

$S_\perp$ (red), $S_{//}$ (blue) and $S_{analytical}$ (green) for cysteine where $p_{observed}$ is maximum: -392 mV in the negative sweep. Acquisition time was 180 s. $S_\perp$ and $S_{//}$ were not baseline-corrected. These spectra constitute the raw data presented for -392 mV in Figure 3.9.

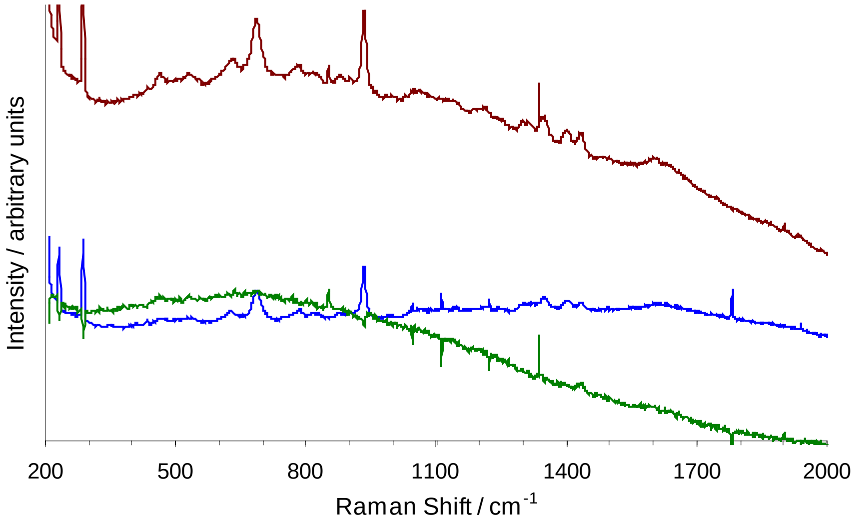

$S_\perp$ (red), $S_{//}$ (blue) and $S_{analytical}$ (green) for cysteine where $p_{observed}$ is minimum: -692 mV in the positive sweep. Acquisition time was 180 s. $S_\perp$ and $S_{//}$ were not baseline-corrected. These spectra constitute the raw data presented for -692 mV in Figure 3.9.

Supplemental Data for Nanohole Arrays in a Copper Film (Chapter 4):

Enhancement Factor Calculation

volume of the benzene cylinder probed by the laser

5	µm = laser spot radius = cylinder radius
470	µm = microscope objective's focal length = cylinder height
3.69E+04	µm^3 = volume of the benzene cylinder probed by the laser
3.69E-14	m^3 = volume of the benzene cylinder probed by the laser
3.69E-11	L = volume of the benzene cylinder probed by the laser

number of benzene molecules in the cylinder

11.25	mol/L = concentration of pure liquid benzene
4.15E-10	mol of benzene in the cylinder
2.50E+14	molecules of benzene in the cylinder

counts per molecule of benzene

17202	counts for benzene's ring-breathing band after 20 s of accumulation
6.88E-11	counts per molecule of benzene

dimensions of oxazine720

2.5	nm long
1	nm wide
0.4	nm thick
1.00E+00	nm^3 = volume of an oxazine720 molecule, assuming it packs as a 2.5 × 1 × 0.4 nm^3 box
1.00E-09	µm^3 = volume of an oxazine720 molecule, assuming it packs as a 2.5 × 1 × 0.4 nm^3 box

dimensions of the oxazine720 cylinder probed by the laser, and the number of oxazine720 molecules inside it

5	µm = laser spot radius = cylinder radius
50	= estimated number of layers of oxazine720 on the copper surface
0.0875	µm = height of 50 layers of tilted oxazine720 = height of the cylinder; tilted because bonding to the surface is through a nitrogen atom (see reference 28 in Chapter 4)
6.87E+09	= number of oxazine720 molecules in the oxaine720 cylinder if oxazine720 packs as a 1.00E-09 µm^3 box

counts per molecule of oxazine720

1959	counts for oxazine720's 596 cm^{-1} band after 20 s of accumulation
2.85E-07	counts per molecule of oxazine720

estimated enhancement factor; this is calculated using a correction factor that accounts for any difference in the quality of the alignment of the optical system

3420 counts from Si standard on the day that benzene data was acquired
1117 counts from Si standard on the day that oxazine720 data was acquired
1.27E+04 = enhancement factor = (2.85E-07 / 6.88E-11) / (3420 / 1117)

FDTD Fieldstrength Contour Maps for $|Ex|^2$ and $|Hy|^2$

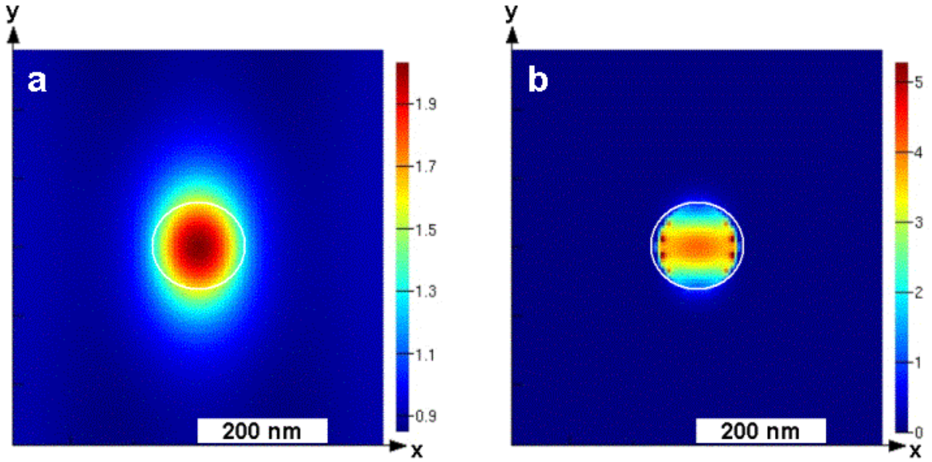

$|Ex|^2$ contours surrounding a hole (centre of the picture) within the 578 nm periodicity array are shown for the backscattering geometry (a) and the forward-scattering geometry (b). Polarization of the incident beam is parallel to the x-axis.

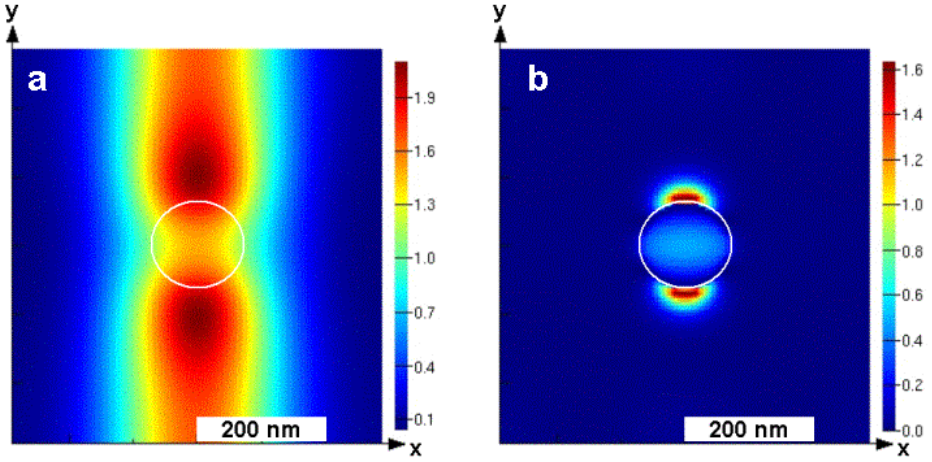

$|Hy|^2$ contours surrounding a hole (centre of the picture) within the 578 nm periodicity array are shown for the backscattering geometry (a) and the forward-scattering geometry (b). Polarization of the incident beam is parallel to the x-axis.

Appendix B: Additional Figures from the Literature Which are Relevant to Our Work on Nanoscale Gratings in a Gold Film (Chapter 5)

Figures from Kahl et al, 1998, *Sensor Actuat. B Chem.*, 51, 285-291

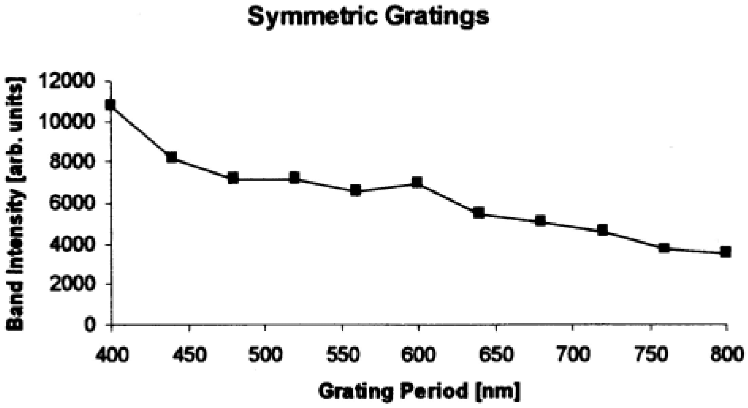

Figure 7 SERS intensity plotted as a function of period for symmetric gratings (groove width = line width). Other details are discussed in Chapter 5.

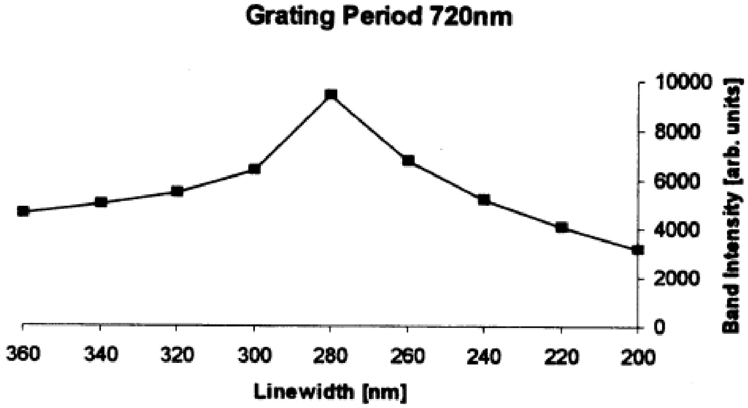

Figure 8 SERS intensity plotted as a function of line width. Groove width + line width = 720 nm. Other details are discussed in Chapter 5.

Reprinted, with permission, from *Sensor Actuat. B Chem.*, 1998, 51, 285-291. Kahl M, Voges E, Kostrewa S, Viets C, Hill W; Periodically Structured Metallic Substrates for SERS. Copyright, 1998, Elsevier.

Figures from Wirgin and Maradudin, 1986, *Prog. Surf. Sci.*, 22, 1, 1-99

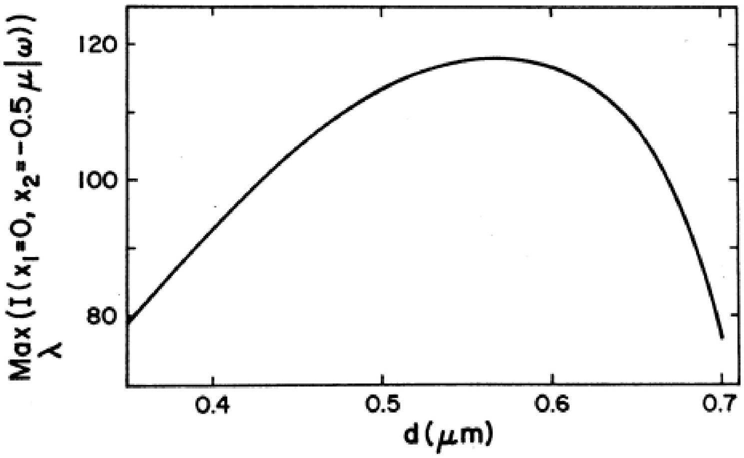

Figure 28 Resonant enhancement plotted as a function of period. Groove width = 350 nm. Other details are discussed in Chapter 5.

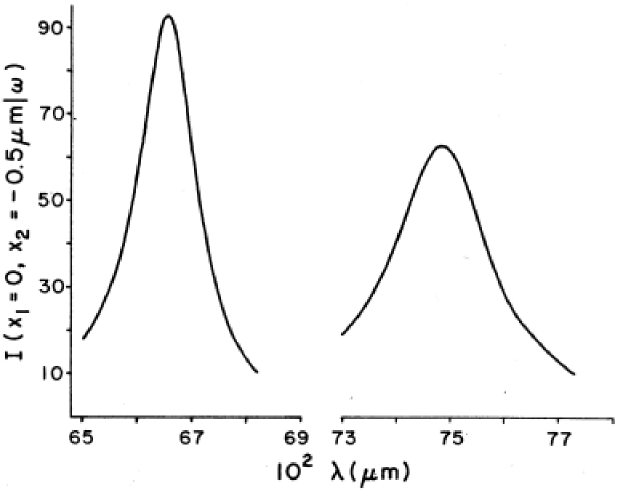

Figure 29 Enhancement plotted as a function of wavelength. Period = 400 nm. Groove width = 350 nm in the plot on the left, and 400 nm ("comb grating") in the plot on the right. Other details are discussed in Chapter 5.

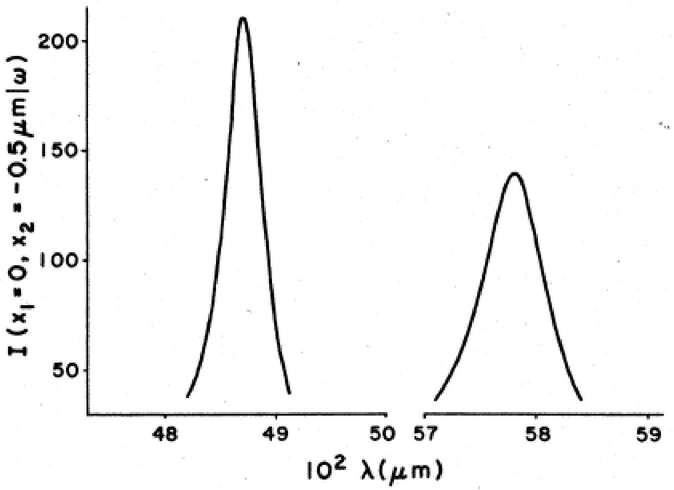

Figure 30 Enhancement plotted as a function of wavelength. Period = 400 nm. Groove width = 250 nm in the plot on the left, and 300 nm in the plot on the right. Other details are discussed in Chapter 5.

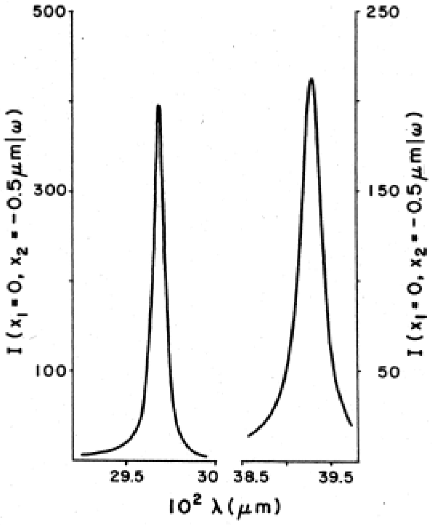

Figure 31 Enhancement plotted as a function of wavelength. Period = 400 nm. Groove width = 150 nm in the plot on the left, and 200 nm in the plot on the right. Other details are discussed in Chapter 5.

Reprinted, with permission, from *Prog. Surf. Sci.*, 1986, 22, 1, 1-99. Wirgin A, Maradudin AA; Resonant Response of a Bare Metallic Grating to s-Polarized Light. Copyright, 1986, Elsevier.